agronomy

MDPI

Article

Identification of Plastic Mulch in Cotton Fields Using UAV-Based Hyperspectral Data and Deep Learning Semantic Segmentation

Qingyao Zhao [1], Shenglin Li [1,2], Fukui Gao [1], Huifeng Ning [1,3], Dongke Dai [1], Pengyuan Zhu [1], Nanfang Li [1], Yinping Song [1], Caixia Li [1,3,*] and Hao Liu [1,3,*]

[1] Key Laboratory of Crop Water Use and Regulation, Ministry of Agriculture and Rural Affairs, Institute of Farmland Irrigation, Chinese Academy of Agricultural Sciences, Xinxiang 453002, China; zhaoqingyao1@126.com (Q.Z.); shenglinli@hist.edu.cn (S.L.); gaofukui1207@163.com (F.G.); ninghuifeng@126.com (H.N.); 15044848958@163.com (D.D.); 82101232120@caas.cn (P.Z.); 18638002993@163.com (N.L.); syp9965@163.com (Y.S.)

[2] School of Information Engineering, Henan Institute of Science and Technology, Xinxiang 453003, China

[3] Shangqiu Agro-Ecological System, National Observation and Research Station, Shangqiu 476000, China

* Correspondence: licaixia@caas.cn (C.L.); liuhao03@caas.cn (H.L.)

Abstract

Plastic mulching is widely used in arid and semi-arid cotton systems to improve soil hydrothermal conditions and water–nutrient use efficiency. However, residual mulch and its potential contribution to microplastic inputs pose growing environmental and soil-quality risks, highlighting the need for high-resolution and automated approaches to support plastic waste management, targeted retrieval, and precision field operations. Taking a mulched cotton field in Alar, Xinjiang, as the study area, this study proposes a novel plastic mulch extraction method that integrates Unmanned Aerial Vehicle (UAV)-based hyperspectral imagery with deep learning semantic segmentation. The Jeffries–Matusita (JM) distance was employed to select highly separable optimal bands and their combinations for discriminating plastic mulch, bare soil, and cotton canopy, which were then used to drive UNet, DeepLabV3+, and PSPNet models for plastic mulch mapping. The results indicate that the PSPNet model driven by the 402 nm single-band reflectance, Normalized Difference Index (NDI) (861 nm, 410 nm), and NDI (757 nm, 676 nm) achieved the best performance for plastic mulch identification (Intersection over Union (IoU) = 80.28%), significantly outperforming the RGB-based model (IoU = 76.51%). This study enables accurate, spatially explicit assessments of residual mulch, providing actionable evidence for plastic waste monitoring and management, while supporting sustainable agriculture and precision farmland management.

Keywords: UAV remote sensing; plastic mulch identification; hyperspectral imagery; Jeffries–Matusita distance; semantic segmentation; mulched cotton fields

Check for updates

Academic Editor: Alberto San Bautista

Received: 16 January 2026
Revised: 11 February 2026
Accepted: 13 February 2026
Published: 15 February 2026

Copyright: © 2026 by the authors. Licensee MDPI, Basel, Switzerland. This article is an open access article distributed under the terms and conditions of the Creative Commons Attribution (CC BY) license.

1. Introduction

Plastic mulching technology has been widely applied across various agricultural systems due to its ability to regulate soil temperature, conserve soil moisture, suppress weed growth, and reduce the incidence of pests and diseases. These advantages substantially enhance crop yield and quality, making plastic mulching an important agronomic practice for ensuring food security and promoting sustainable agricultural development [1–3]. Consequently, this technology has been intensively adopted in major maize and cotton production regions in Northwest China, tobacco-growing areas in Southwest China, as

well as in vegetable-producing regions nationwide [4]. China has long ranked among the world's leading countries in terms of plastic mulch consumption and mulched area, with plastic film usage increasing from approximately 0.8 million tons in 2000 to a peak of about 1.5 million tons in 2016, accounting for nearly 10% of the national sown area [5]. In particular, due to arid and cold climatic conditions, the mulching ratio exceeds 80% in Northwest China and surpasses 90% in Xinjiang [6]. However, with prolonged and increasing use, coupled with difficulties in film recovery and recycling [7], residual plastic pollution has become increasingly severe, and the contamination of farmland soils and agro-ecosystems by plastic residues has emerged as a critical challenge to sustainable agricultural development [8–11]. Numerous studies have demonstrated that the long-term accumulation of non-degradable plastic films in agricultural soils can reduce soil porosity, hinder air–water transport, and even alter soil salinity migration patterns, thereby deteriorating the crop root-zone environment [12,13]. Meanwhile, mulched surfaces exhibit spectral characteristics and energy partitioning patterns that differ markedly from those of bare soil, implying that interannual and regional variations in plastic mulch coverage may further affect the accuracy of land surface process studies and remote sensing monitoring. Therefore, achieving accurate and automated acquisition of the spatiotemporal distribution of plastic mulch at the regional scale has become a key issue that urgently needs to be addressed in agricultural management, residual plastic pollution control, and quantitative remote sensing analysis.

Traditional investigations of plastic mulch mainly rely on field surveys and ground-based measurements, which are labor-intensive and inefficient and thus unable to satisfy the demand for large-scale, continuous, and dynamic monitoring. In contrast, remote sensing techniques enable rapid and accurate observations over large areas and have attracted extensive research attention [14,15]. Early studies primarily employed medium- to low-resolution satellite data, such as Landsat and MODIS. Hasituya et al. [16] demonstrated through feature analysis of Landsat-8 OLI imagery that spectral characteristics are the primary contributors to plastic mulch identification. Subsequent studies [17,18] further investigated the spatiotemporal stability of polarization scattering intensity, polarimetric decomposition features, and decision tree classifiers in plastic mulch detection. In addition, time-series data [19], optimal spatial scale selection [20], and multi-temporal data fusion approaches [21] have been explored to improve the accuracy of plastic mulch monitoring. However, medium- to low-resolution satellite remote sensing approaches suffer from inherent limitations. Insufficient spatial resolution frequently leads to mixed pixels and spectral confusion among plastic mulch, bare soil, and bright background vegetation. Moreover, the spectral characteristics of plastic mulch are highly sensitive to film thickness, aging, and surface dust, particularly during rapid crop growth stages such as the squaring and early flowering–boll formation stages of cotton, when dynamic variations in mulch exposure can easily cause identification errors. Consequently, despite their strong potential at the regional scale, satellite-based methods remain inadequate for high-precision, high-resolution mulch assessment at the field scale and for fine agricultural management.

Unmanned aerial vehicle (UAV) remote sensing has emerged as an important data source for plastic mulch identification in recent years [22], owing to its high mobility, flexible imaging schedules, and ultra-high spatial resolution. The centimeter-level resolution provided by UAV platforms enables clear delineation of mulch boundaries, damage patterns, and exposure levels, thereby fundamentally alleviating the mixed-pixel problem associated with medium-resolution satellite imagery. Moreover, UAV-based data acquisition allows flexible selection of imaging timing, effectively avoiding periods with wet mulch surfaces and strong specular reflection, which contributes to improved data quality and identification accuracy. Previous studies have employed UAV-based visible, mul-

tispectral, and even hyperspectral imagery for plastic mulch monitoring. For example, Huang Huacheng et al. [23] proposed a plastic mulch identification method based on UAV hyperspectral imaging. Wu Xuemei et al. [24] conducted residual plastic film detection at different growth stages using an 18–55 m UAV remote sensing platform, combining grayscale differences in visible RGB images and HSV color space components with threshold segmentation and image morphological operations. However, these methods generally lack explicit exploitation of spectral differences for feature construction, resulting in limited sensitivity to fine-scale morphological details and spectral variability of plastic mulch under complex farmland backgrounds. Consequently, their ability to further overcome accuracy bottlenecks remains constrained.

With the rapid advancement of deep learning, semantic segmentation networks have become mainstream approaches for land cover classification owing to their end-to-end learning capability, automatic extraction of discriminative features, and pixel-level classification. Models such as FCN, U-Net, SegNet, and the DeepLab series have been widely applied in agricultural remote sensing, including farmland object extraction, crop identification, and canopy structure analysis [25–29]. The introduction of the FCN model in 2015 opened a new direction for addressing densely annotated semantic segmentation tasks [30,31] and demonstrated superior performance over traditional machine learning approaches in UAV remote sensing image classification [32]. For instance, Fu et al. [33] reported that FCN outperformed traditional support vector machines and patch-based deep convolutional neural networks (DCNNs) in classifying multi-view UAV-acquired remote sensing images. Subsequent studies further explored the application of FCN-based architectures, including the use of U-Net [34] for information extraction from infrared UAV data and non-downsampling FCN models for labeling high-resolution imagery [35]. Notably, in plastic mulch identification tasks, spectral signatures are highly sensitive to temporal variation, dust accumulation, and material optical properties, making handcrafted features difficult to generalize across diverse farmland conditions. In contrast, deep learning methods can automatically learn texture, color, and edge features of plastic mulch from large-scale datasets, substantially enhancing classification accuracy under complex background environments. Consequently, deep learning-based semantic segmentation offers a high-precision and robust solution for plastic mulch monitoring.

However, existing UAV-based studies rarely integrate spectral separability analysis with deep semantic segmentation in an interpretable framework, particularly for discriminating plastic mulch from bare soil under varying crop growth stages. To fill this gap, we propose an interpretable, integrated "separability analysis–feature selection–semantic segmentation" framework. Using UAV-based hyperspectral imagery, the spectral separability among plastic mulch, bare soil, and crop canopy was systematically analyzed, and optimal band combinations were identified using the Jeffries–Matusita (JM) distance. During dataset construction, diverse samples covering different growth stages and canopy coverage conditions were incorporated to enhance model robustness. Classical deep semantic segmentation networks were employed as baseline architectures, and attention mechanisms, multi-scale atrous convolutions, skip connections, and attention-enhancement modules were integrated to improve plastic mulch feature extraction. By evaluating the contributions of different spectral bands and their combinations to classification performance, a high-precision plastic mulch identification model suitable for the complex farmland environments of Xinjiang was developed. This study systematically reveals the spectral differentiation characteristics of typical land cover types in mulched cotton fields. Specifically, we develop a Jeffries–Matusita (JM) distance-driven band/index selection strategy that quantitatively explains the sources of separability among plastic mulch, bare soil, and crop canopy. Building on this, we establish a JM-based band selection approach and

construct a high-accuracy semantic segmentation model for plastic mulch identification, providing critical technical support and valuable references for UAV remote sensing applications in residual plastic pollution monitoring, mulch coverage assessment, and precision agricultural management.

2. Materials and Methods

2.1. Study Area and Experimental Design

Field experiments were conducted from April to October during 2024–2025 at the Alar Modern Agricultural Comprehensive Experimental Station in Xinjiang, China (81°17′56.52″ E, 40°32′36.90″ N; elevation: 1014 m), as shown in Figure 1. The station is located in a plain desert–oasis region near the Tarim River Basin and is characterized by a warm temperate, extremely continental arid desert climate, featuring dry summers, low precipitation, abundant solar radiation, strong evaporation, and large diurnal temperature variations. The annual surface evaporation is approximately 2000 mm, relative humidity ranges from 47% to 60%, the long-term mean annual temperature is 11.3 °C, and the accumulated temperature ranges from 3450 to 4432 °C. The experimental field is composed of sandy loam soil with good aeration, and the groundwater table depth exceeds 3 m. The region is rich in light and thermal resources, and agricultural production relies entirely on irrigation [36]. Plastic mulch is extensively used in the study area, with cotton as the primary crop. The planting pattern follows a one-film–three-belt–six-row configuration (Figure 2). To improve the generalizability of the model, mulched cotton fields under different experimental treatments and canopy coverage conditions were selected for data acquisition.

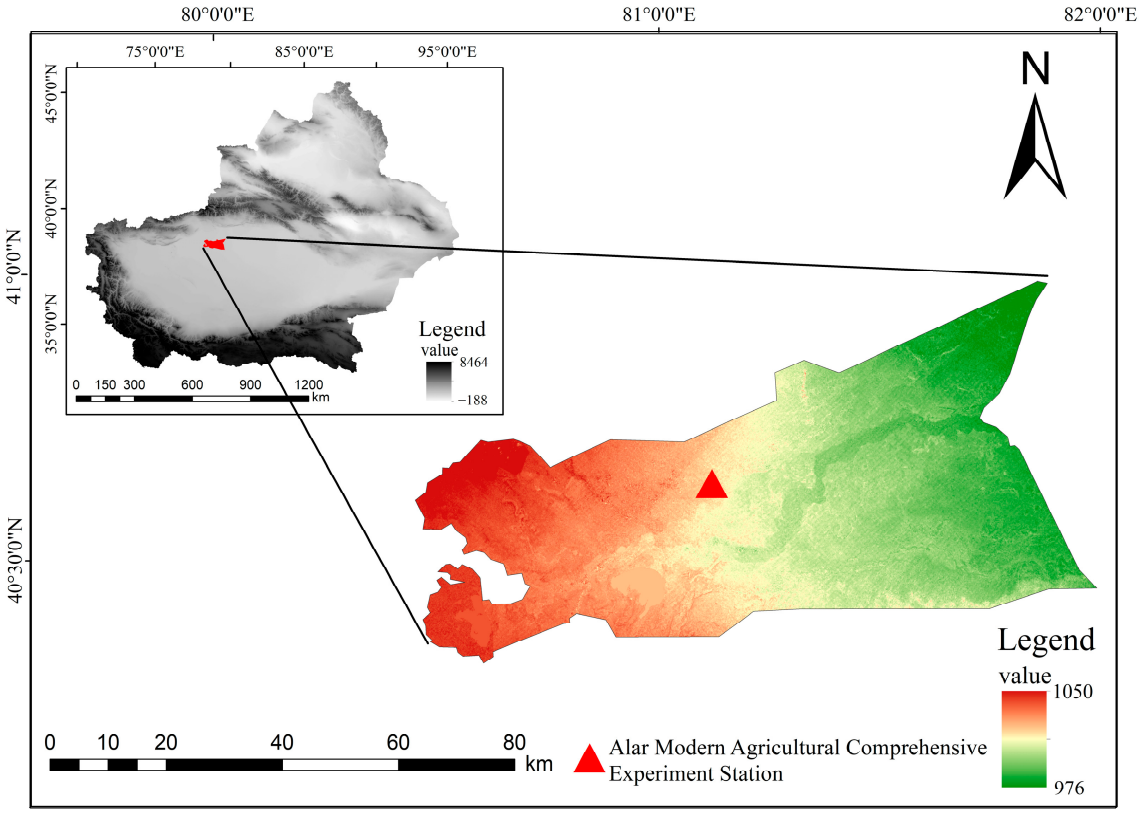


Figure 1. Location and overview of the study area in Alar, Xinjiang, China.

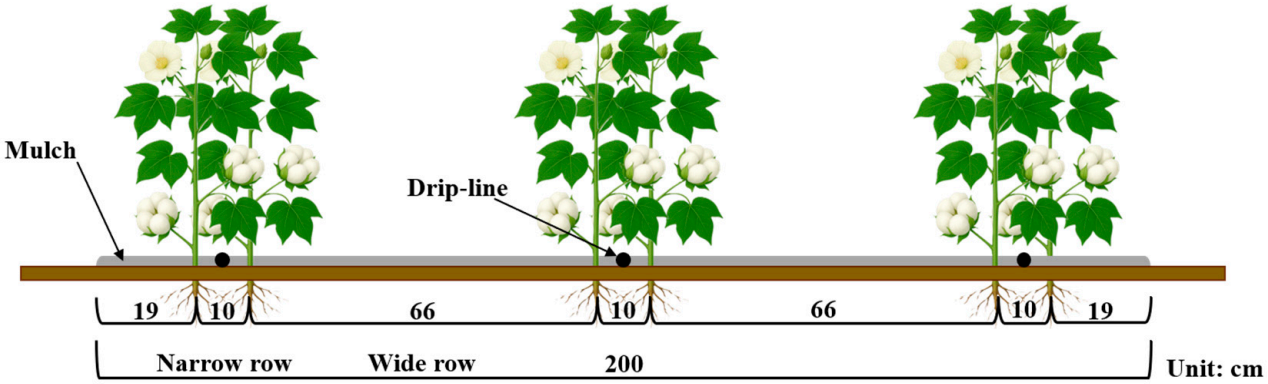


Figure 2. Schematic diagram of the cotton planting pattern.

2.2. Data Acquisition and Preprocessing

2.2.1. UAV Data Acquisition

UAV-based hyperspectral images were acquired during each experimental campaign. An M600 Pro UAV (DJI, Inc., Shenzhen, Guangdong, China) equipped with a Pika L hyperspectral camera (Resonon, Inc., Bozeman, MA, USA) was used as the remote sensing platform. The hyperspectral system comprises 150 spectral bands covering a wavelength range of 400–1000 nm, with an approximate spectral resolution of 5 nm. Owing to the integration of a high-precision inertial measurement unit, the sensor is capable of acquiring high-quality hyperspectral imagery.

UAV data were collected on 29 June, 10 July, 17 July, 26 July, and 12 August in 2024, and on 6 July, 13 July, 20 July, 4 August, and 11 August in 2025. For each mission, the UAV was operated at an altitude of 40 m with a flight speed of 3 $m \cdot s^{-1}$. The forward and side overlaps were set to 30% and 40%, respectively. All flights were conducted between 13:00 and 15:00 under clear, cloud-free, and windless conditions. The takeoff location, flight trajectory, and flight altitude were maintained consistently across all missions. Ground reference calibration panels were imaged during each flight for spectral reflectance calibration. Each flight lasted approximately 20 min, during which solar irradiance variations were minimal; therefore, atmospheric correction was not performed. The UAV platform and imaging system used for data acquisition are shown in Figure 3.



Figure 3. DJI M600 Pro unmanned aerial vehicle (**left**) and Pika L hyperspectral imager (**right**).

2.2.2. Data Preprocessing

The preprocessing of hyperspectral imagery included flight-line clipping, geometric correction, georeferencing, image mosaicking, hyperspectral cube generation, and reflectance calculation. Hyperspectral image processing was conducted using MegaCube 2.15, ArcGIS 10.8, and ENVI 5.3 software packages. Reflectance values for each spectral band were obtained, covering a wavelength range of 400–1000 nm.

2.3. Band Separability Analysis

Single-Band Separability Analysis

In this study, the JM distance was employed to evaluate the separability of all individual spectral bands within the wavelength range of 400–1000 nm. The JM distance was calculated using the following equation:

$$JM_{ij} = 2\left(1 - e^{-B_{ij}}\right) \tag{1}$$

$$B_{ij} = \frac{1}{8}(\mu_i - \mu_j)^T \left(\frac{\Sigma_i + \Sigma_j}{2}\right)^{-1} (\mu_i - \mu_j) + \frac{1}{2}\ln\left[\frac{\left|\frac{\Sigma_i+\Sigma_j}{2}\right|}{\sqrt{|\Sigma_i||\Sigma_j|}}\right] \tag{2}$$

where μ_i and μ_j are the mean vectors of the spectral samples for classes i and j, respectively, Σ_i and Σ_j are the corresponding covariance matrices.

The JM distance reflects the degree of separability between two classes in spectral space and ranges from 0 to 2, where JM values greater than 1.9 indicate high inter-class separability, whereas values lower than 1.0 suggest weak discriminative capability of the spectral band [37]. In the calculation process, class mean vectors and covariance matrices were first estimated based on the reflectance distributions of representative samples, and the JM distance was then derived from the Bhattacharyya distance. By computing the JM distance on a band-by-band basis for the canopy–mulch, mulch–soil, and canopy–soil class pairs, the variation patterns of spectral separability across different bands and growth stages were analyzed, and sensitive bands with higher contributions to plastic mulch identification were subsequently identified.

To construct two-band spectral indices with high separability, four commonly used indices were selected in this study, including the difference index (DI), ratio index (RI), normalized difference index (NDI), and logarithmic ratio index (LRI) [38]. The JM distance was consistently employed as the evaluation criterion to identify optimal band combinations with high separability. The four spectral indices were calculated as follows:

$$DI = R_{\lambda 1} - R_{\lambda 2} \tag{3}$$

$$RI = \frac{R_{\lambda 1}}{R_{\lambda 2}} \tag{4}$$

$$NDI = \frac{R_{\lambda 1} - R_{\lambda 2}}{R_{\lambda 1} + R_{\lambda 2}} \tag{5}$$

$$LRI = \log\left(\frac{R_{\lambda 1}}{R_{\lambda 2}}\right) \tag{6}$$

where R_{λ_i} denotes the spectral reflectance at wavelength λ_i. In this study, a matrix-based approach was employed to exhaustively construct spectral indices by pairing all possible band combinations across the full spectral range. The JM distance was then calculated between the corresponding class pairs, and JM value heatmaps were generated to visualize the separability patterns. Based on the separability levels reflected by the JM values, optimal spectral indices were subsequently selected.

2.4. Semantic Segmentation Model Construction

2.4.1. Dataset Preparation

To construct a semantic segmentation dataset for plastic mulch identification in mulched cotton fields, RGB bands were extracted from 10 UAV hyperspectral images and used to generate visible color images (512 × 512 pixels). Manual annotation was conducted by creating shapefile (shp) polygons to label the visible images, which were categorized into three classes: cotton canopy, exposed plastic mulch, and bare soil. Given the

high spatial resolution of the UAV imagery, mixed pixels were assumed to be negligible for the plastic mulch identification task. The annotated shapefiles were used as ground-truth labels for semantic segmentation, and an example of the label file is presented in Figure 4. In total, we plotted approximately 2134 (canopy), 895 (bare earth), and 1358 (mulch) polygon areas for these three types of labels. To strengthen data quality and inter-annotator consistency, a dedicated quality-control step was conducted: an independent reviewer re-checked a randomly selected 10% subset of the annotated images, focusing on class assignment consistency and boundary delineation. Disagreements—primarily occurring along blurred boundaries and visually mixed transition areas—were resolved by consensus following a unified labeling guideline, and the corresponding masks were updated accordingly.

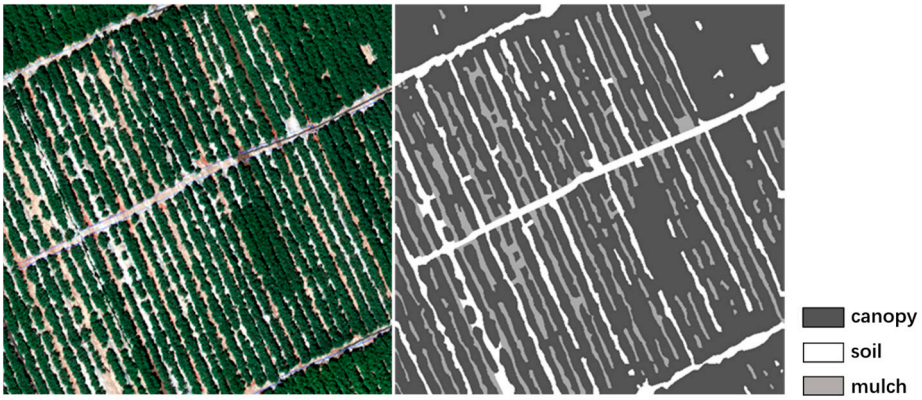


Figure 4. Visible-color image (**left**) and corresponding manual annotation (**right**).

To adapt to complex field environments and enhance the generalization ability, robustness, and learning capacity of the model, multiple data augmentation techniques were applied to the UAV remote sensing images, including sliding-window cropping, salt-and-pepper noise addition, blurring, rotation, brightness adjustment, and random cropping. Through this process, a total of 2000 images were generated. The dataset was randomly divided into training, validation, and test sets at a ratio of 7:2:1, resulting in 1400 training images, 400 validation images, and 200 test images. The training and validation sets were used for model training, while the test set was reserved for independent model evaluation.

2.4.2. Semantic Segmentation Algorithms

DeepLabV3+ is an advanced semantic segmentation network based on an encoder–decoder architecture and represents an improved version of the DeepLab series. Its encoder incorporates the Atrous Spatial Pyramid Pooling (ASPP) module, which employs atrous convolutions with different dilation rates to capture multi-scale contextual information while enlarging the receptive field without reducing feature map resolution. The decoder fuses low-level features and performs progressive upsampling to refine object boundaries and recover spatial details. This architecture has shown strong performance in complex agricultural scenes, enabling effective discrimination of crop canopy, bare soil, and shadowed areas in UAV imagery.

U-Net is a representative fully convolutional network originally developed for medical image segmentation but has been widely adopted in remote sensing and agricultural image analysis due to its simple structure, computational efficiency, and strong transferability. It employs a symmetric encoder–decoder architecture with skip connections between corresponding layers to fuse low- and high-level features, ensuring accurate localization and preservation of boundary details. Owing to its stable training behavior, U-Net is particularly suitable for UAV image segmentation tasks with limited training samples and enables fine-scale identification of cotton canopy, plastic mulch, and bare soil.

PSPNet introduces a Pyramid Pooling Module to capture global contextual information by performing pooling operations at multiple spatial scales. The multi-scale features are subsequently upsampled and concatenated to produce dense prediction results with global consistency. PSPNet demonstrates good generalization performance in high-resolution UAV imagery, particularly for identifying subtle texture variations and changes in vegetation coverage in agricultural environments.

2.4.3. Model Training

The experiments were conducted on a workstation equipped with an Intel(R) Core(TM) i7-10875H CPU, an NVIDIA GeForce RTX 2060 GPU, 6 GB memory, running Windows 10. All deep learning models were implemented using the PyTorch 2.4.1 framework with Python 3.8, and the detailed training hyperparameters are summarized in Table 1. Notably, the initial learning rate for PSPNet was set to 1×10^{-4}, whereas DeepLabV3+ and U-Net used 3×10^{-4}, because PSPNet (with a ResNet-50 backbone and a pyramid pooling head) was more sensitive to the optimization step size and showed less stable early-stage training when using 3×10^{-4} in preliminary runs. Therefore, we adopted a slightly smaller initial learning rate for PSPNet to ensure stable convergence while keeping the remaining settings consistent across models.

Table 1. Training hyperparameters.

Item	PSPNet	DeepLabV3+	U-Net
Framework		Pytorch	
Backbone	ResNet-50	MobileNetV2	VGG
Initialization checkpoint	pspnet_resnet50.pth	deeplab_mobilenetv2.pth	unet_vgg_voc.pth
Input size		128×128	
Effective init LR	1×10^{-4}	3×10^{-4}	3×10^{-4}
Scheduler		Cosine	
Epochs (freeze/unfreeze)		100 (50/50)	
Batch (freeze/unfreeze)		8/4	
FP16		Yes	
Early stopping		No	

2.4.4. Semantic Segmentation Evaluation

In this study, the mean Intersection over Union (mIoU) was employed to evaluate the effectiveness of the semantic segmentation models [39] in distinguishing plastic mulch, crop canopy, and bare soil. The main calculation formula is given as follows:

$$\text{mIoU} = \frac{1}{N}\sum_{i=1}^{N}\frac{TP_i}{TP_i + FP_i + FN_i} \tag{7}$$

where $N = 3$ denotes the number of classes in this study, TP_i represents the number of pixels correctly classified as class i, FP_i denotes the number of pixels incorrectly classified as class i, and FN_i represents the number of pixels belonging to class i but misclassified as other classes. The mean Intersection over Union (mIoU) measures the degree of overlap between predicted results and ground-truth labels for each class and is widely used as a comprehensive evaluation metric in semantic segmentation. In the three-class scenario ($N = 3$), the mIoU is obtained by computing the IoU for each class (e.g., canopy, bare soil, and plastic mulch) and then averaging the values across all classes.

3. Results and Analysis

3.1. Spectral Reflectance of Single Bands

Figure 5 presents the reflectance spectra of plastic mulch, bare soil, and cotton canopy in the wavelength range of 400–1000 nm on representative observation dates during the cotton growing seasons of 2024 and 2025. Overall, the three land cover types exhibit good separability across the entire spectral range, while their spectral shapes show clear stage-dependent characteristics along the crop growth process. In particular, canopy reflectance displays a sharp increase around 700 nm, serving as a key spectral feature for distinguishing canopy from other surface types. Reflectance rapidly increases from approximately 0.05 in the visible region to 0.45–0.60 in the near-infrared region, making the canopy the most pronounced and stable class among the three. In contrast, the reflectance of plastic mulch remains consistently higher than that of bare soil throughout all growth stages and shows a smooth increasing trend across both the visible and near-infrared regions, with values ranging from approximately 0.10 to 0.40. Compared with bare soil, plastic mulch exhibits a faster and higher reflectance increase in the visible region (400–700 nm), while its near-infrared reflectance (approximately 0.35–0.50) is distinctly lower than that of the canopy but higher than that of bare soil. Bare soil reflectance, although consistently lower than that of plastic mulch, follows a similar increasing trend, with values of approximately 0.07–0.25 in the visible region and reaching about 0.25–0.35 beyond 750 nm. These hyperspectral reflectance characteristics observed across different dates indicate good separability among plastic mulch, bare soil, and canopy from the visible to near-infrared regions, providing a clear foundation for subsequent selection of highly separable spectral bands and construction of two-band indices.

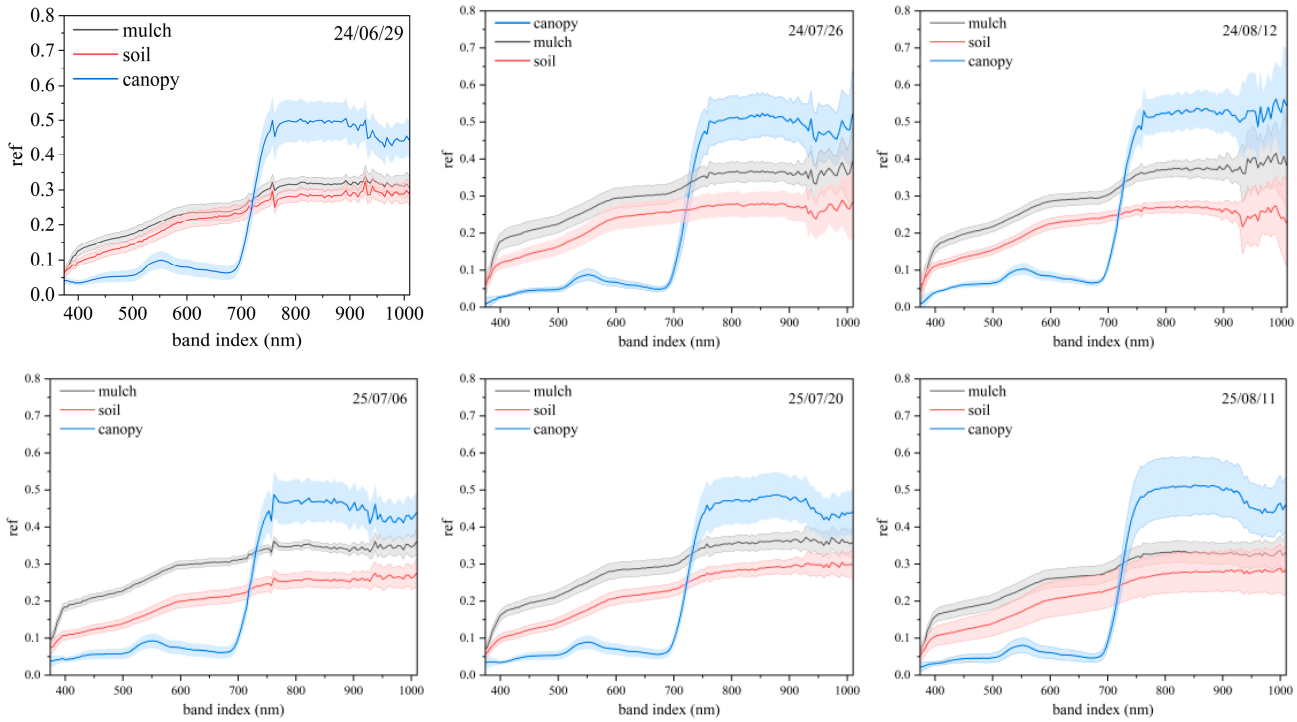


Figure 5. Single-band reflectance at different growth stages.

3.2. Single-Band JM Distance Analysis

Figure 6 shows the JM distance curves for different observation dates. Higher JM values indicate stronger spectral separability between classes. On most dates, the JM values for the mulch–soil class pair reach a peak around 400 nm in the visible region, followed by a gradual decrease with increasing wavelength and a minimum at approximately 720 nm.

The JM values then increase and remain relatively stable in the 750–900 nm range before declining again in the 900–1000 nm range. Overall, the separability between plastic mulch and bare soil is relatively high in the 400–500 nm and 750–900 nm wavelength ranges. The mulch–canopy and soil–canopy class pairs exhibit similar JM variation patterns across the 400–1000 nm spectral range, with JM values close to 2.0 in the visible region and remaining relatively high (approximately 1.75) in the near-infrared region between 750 and 900 nm. These results indicate that both plastic mulch–canopy and bare soil–canopy pairs show stronger separability in the visible spectral region. Among the three class pairs, plastic mulch and canopy exhibit the strongest separability, whereas bare soil and plastic mulch show the weakest separability, which is consistent with the spectral characteristics observed in the hyperspectral reflectance curves.

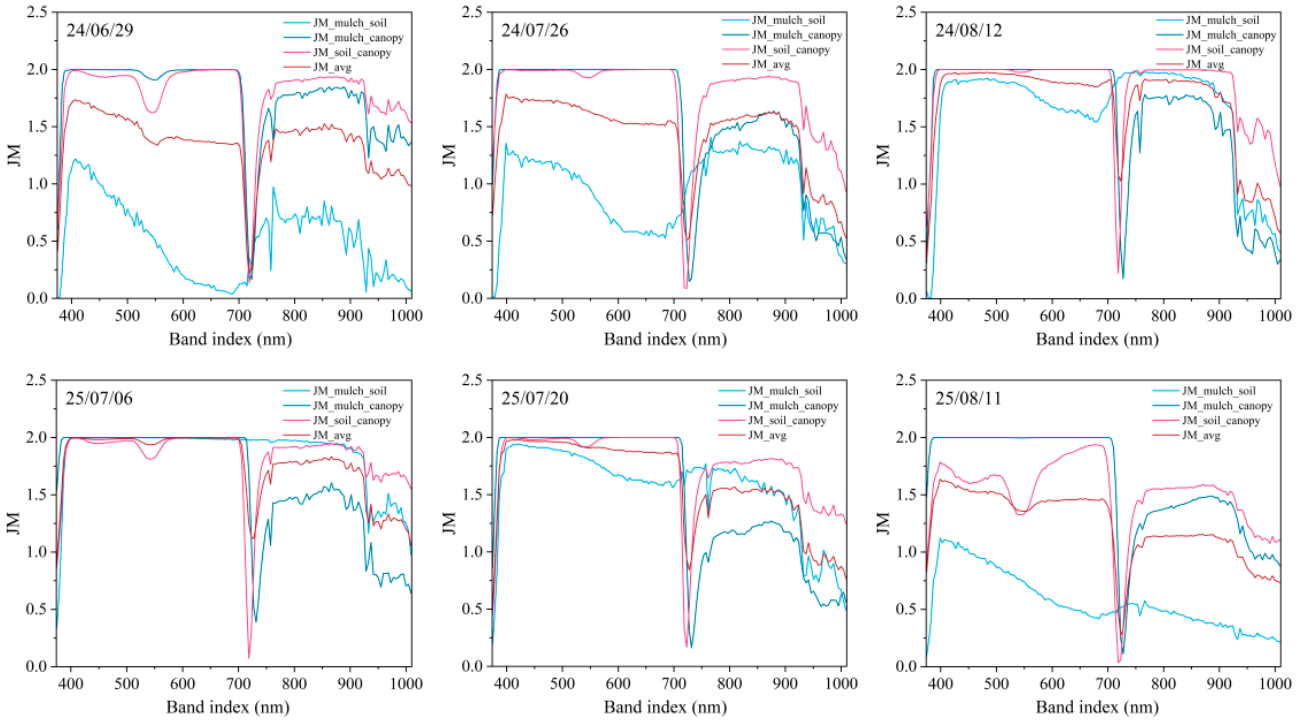
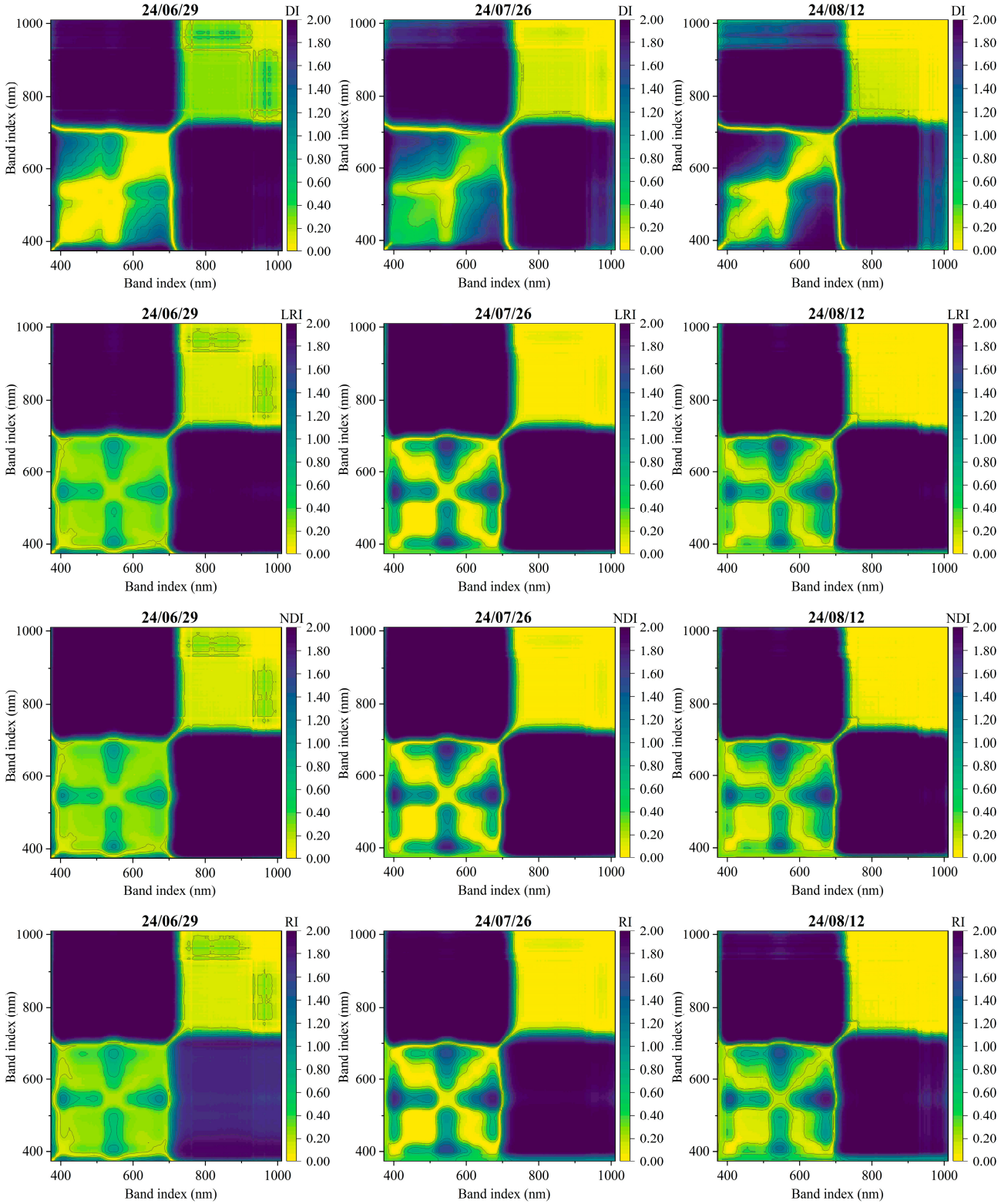


Figure 6. Single-band JM values at different observation dates.

3.3. JM Distance Analysis of Two-Band Indices

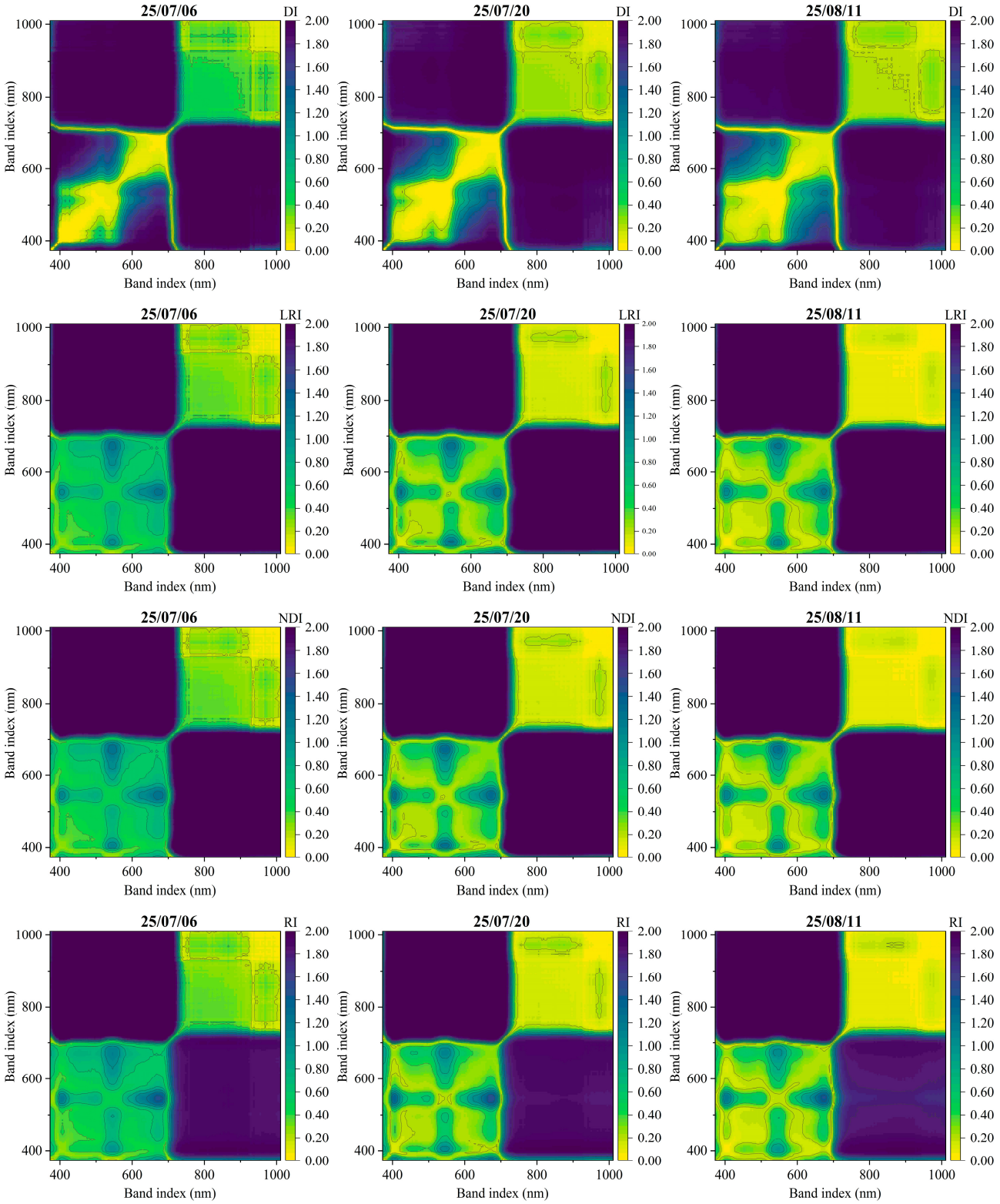
To further enhance the separability between plastic mulch and canopy in hyperspectral imagery, four two-band indices—including the difference index (DI), logarithmic ratio index (LRI), normalized difference index (NDI), and ratio index (RI)—were constructed using all possible combinations of the 150 effective spectral bands. The corresponding JM distances were calculated to evaluate the separability of these two-band indices among different classes.

Figure 7 illustrates the JM contour maps of the four indices for the mulch–canopy class pair on six observation dates in 2024 and 2025. Overall, the JM contour patterns of the four reflectance-based indices are highly similar, with optimal separability consistently observed in band combinations involving the visible (400–700 nm) and near-infrared (700–1000 nm) regions, where JM values remain close to 2.0. Among the four indices, LRI, NDI, and RI exhibit more similar contour patterns, suggesting that these three indices provide comparable improvements in enhancing the separability of single-band reflectance.



(**a**) Two-band spectral indices in 2024

Figure 7. *Cont*.

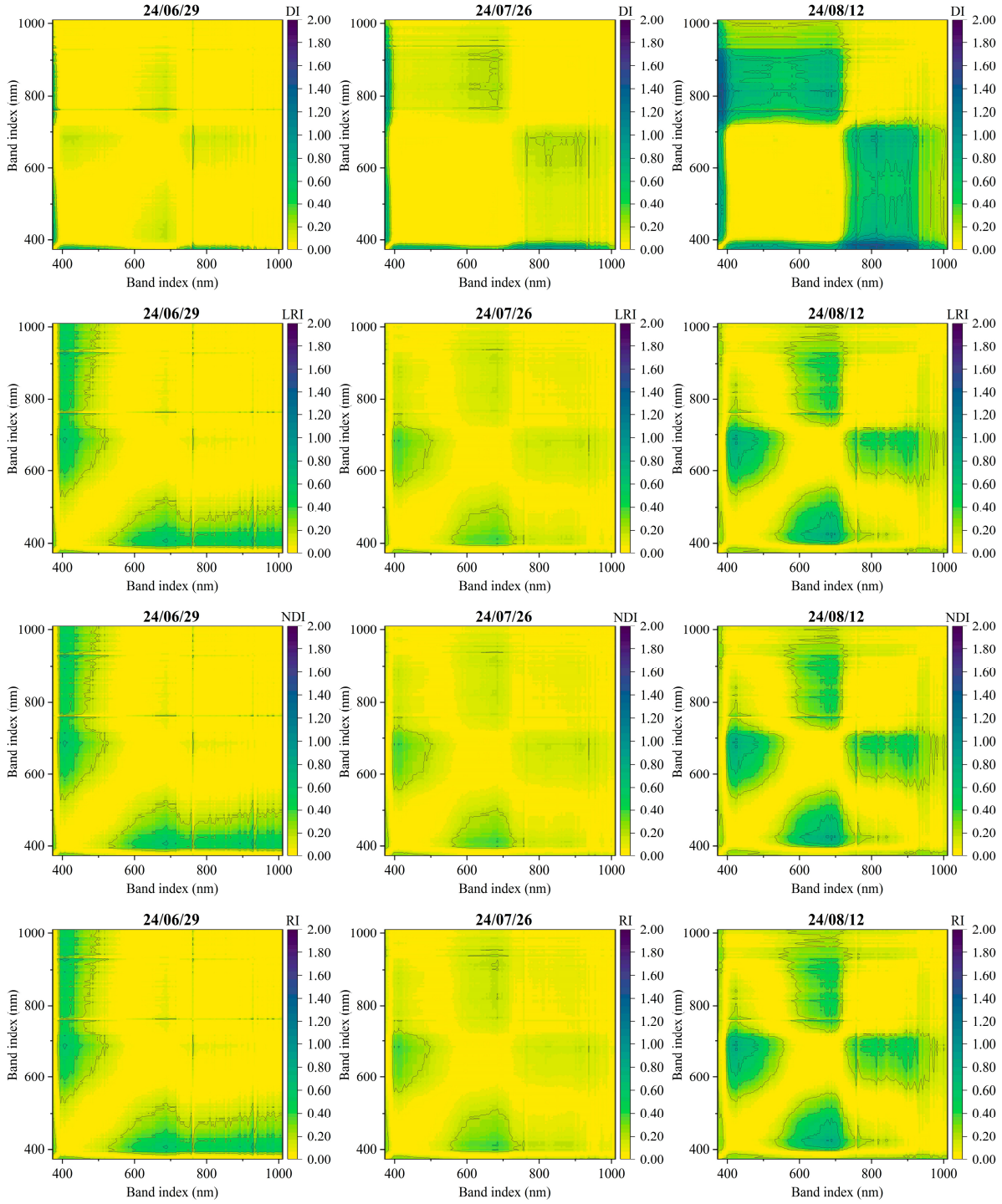


(**b**) Two-band spectral indices in 2025

Figure 7. Contour maps of JM values for two-band spectral indices between plastic mulch and canopy.

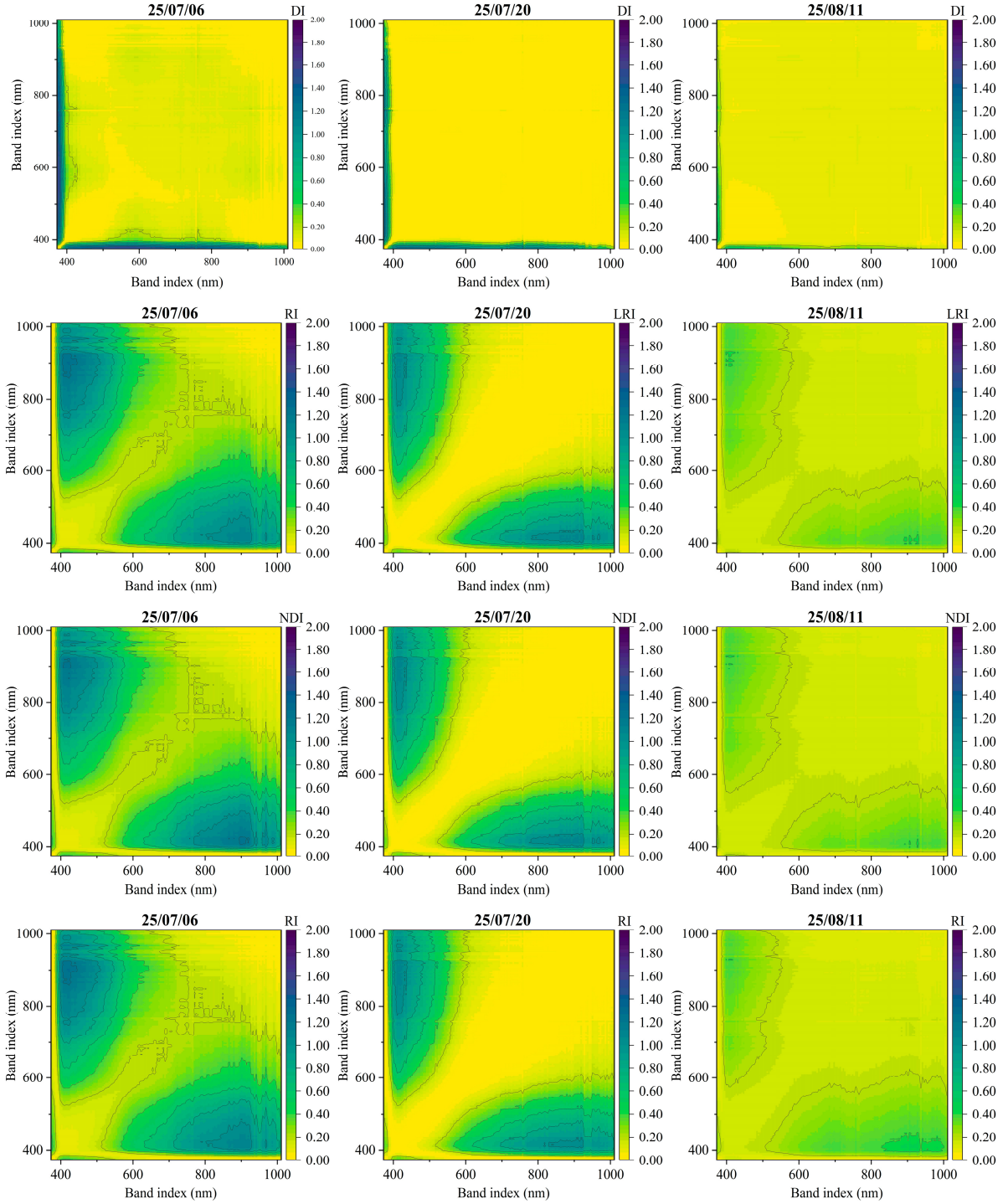
As shown in Figure 8, because the reflectance differences between plastic mulch and bare soil are relatively weak across the 400–1000 nm spectral range, the JM values of reflectance-based two-band indices for the mulch–soil class pair are generally low, indicating that two-band indices have limited effectiveness in constructing discriminative features for this class pair. Relatively higher JM values are mainly concentrated in band

combination regions involving wavelengths around 400 nm and 650 nm in the visible spectrum, suggesting that differences in blue and red reflectance between plastic mulch and bare soil are more pronounced.



(**a**) Two-band spectral indices in 2024

Figure 8. *Cont.*

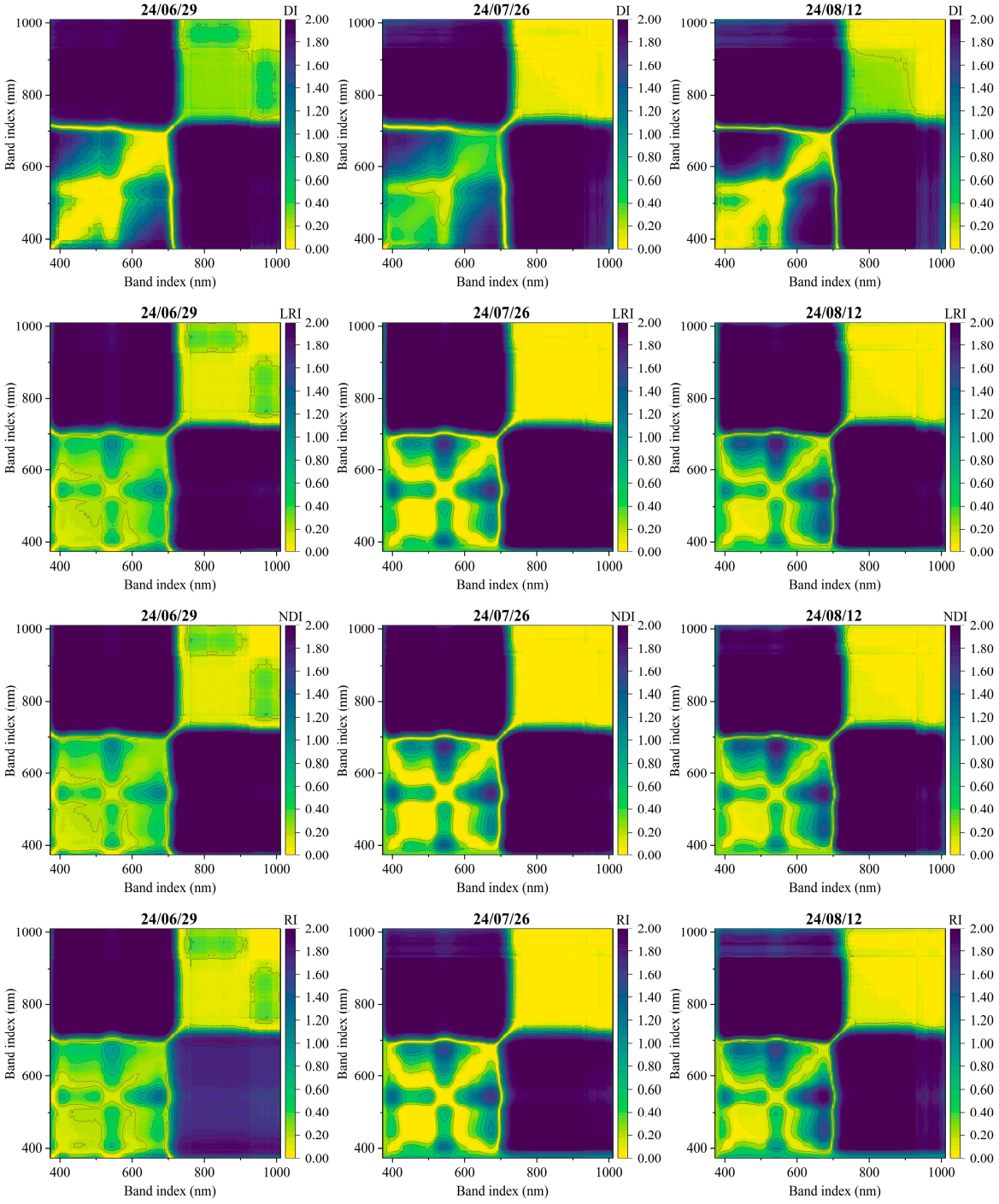


(**b**) Two-band spectral indices in 2025

Figure 8. Contour maps of JM values for two-band spectral indices between plastic mulch and bare soil.

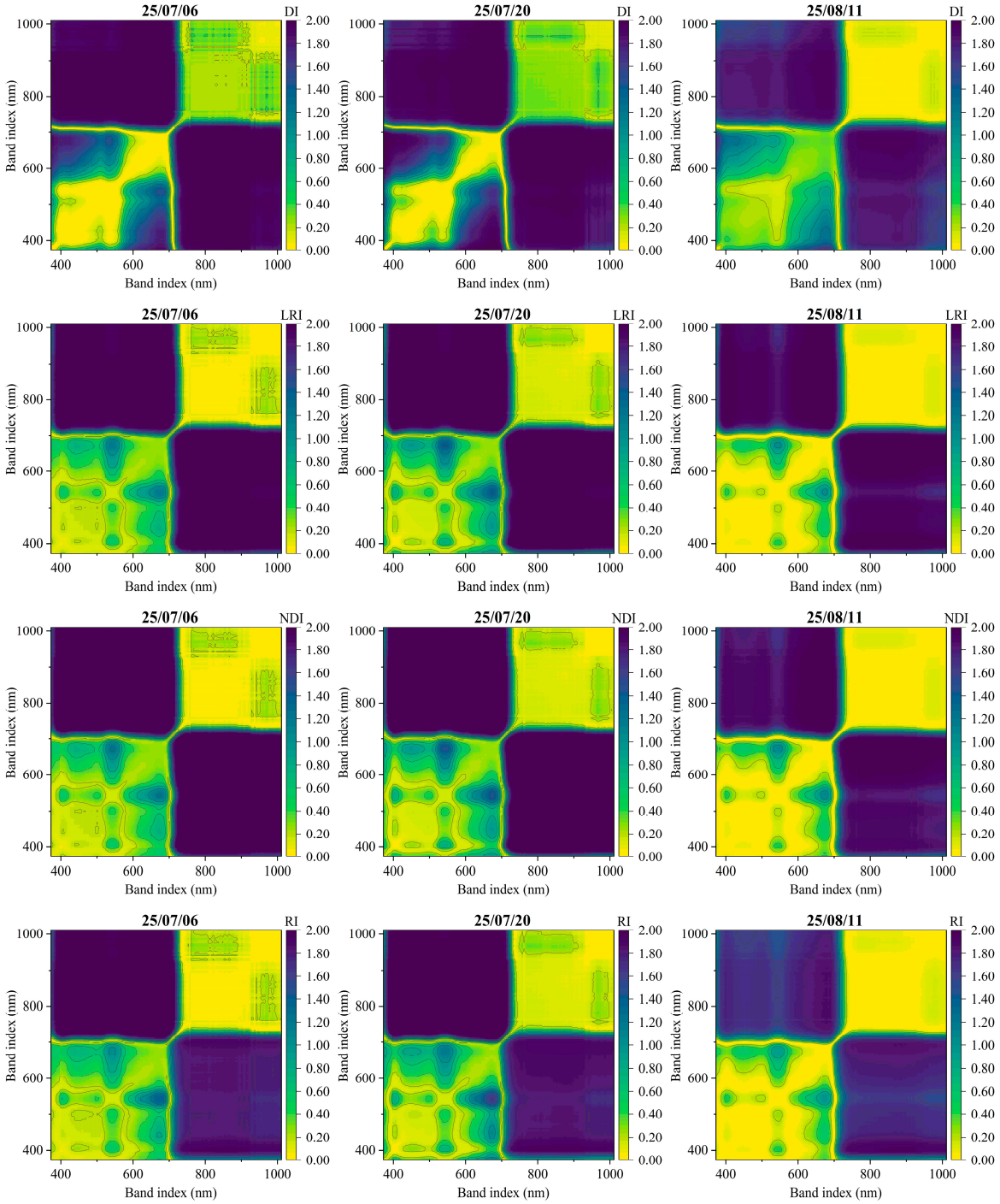
As shown in Figure 9, the variation patterns of the JM value heatmaps for two-band indices between bare soil and canopy are consistent with those observed for the mulch–canopy class pair. Although the two-band index heatmaps for all three class pairs exhibit clear growth-stage-dependent differences, the regions with the highest JM values remain generally consistent across different periods, with the difference index (DI) showing the most pronounced deviation from the other indices. Overall, DI-based band combinations in the visible spectral range exhibit stronger stage sensitivity, with high-JM regions undergoing noticeable morphological changes in response to variations in canopy structure.

In contrast, indices such as LRI, NDI, and RI display more stable and continuous high-value regions, particularly for band combinations between 600–650 nm and 700–800 nm, which consistently maintain high discriminative capability. These differences indicate that DI emphasizes local slopes and abrupt changes in spectral curves and is therefore more sensitive to variations in leaf structure and moisture dynamics during different growth stages, whereas the other indices, owing to their ratio-based, logarithmic, or normalization-based formulations, exhibit higher temporal robustness. Consequently, although the JM heatmaps of the three class pairs show growth-stage-dependent variations across different dates, their core high-separability band combinations largely overlap, indicating shared spectral discriminative capability among bare soil, plastic mulch, and canopy.



(**a**) Two-band spectral indices in 2024

Figure 9. *Cont*.



(**b**) Two-band spectral indices in 2025

Figure 9. Contour maps of JM values for two-band spectral indices between bare soil and canopy.

Based on the above analyses, the single-band reflectance around 402 nm was selected as the optimal spectral feature for distinguishing the plastic mulch–bare soil class pair, while the normalized difference index NDI (861 nm, 410 nm) and NDI (757 nm, 676 nm) were identified as the optimal spectral indices for the plastic mulch–canopy and bare soil–canopy class pairs, respectively. Using these selected features, a three-channel optimal spectral composite was constructed as the input dataset for semantic segmentation-based plastic mulch identification, and a three-channel RGB visible image dataset was additionally prepared for comparison.

3.4. Validation Analysis of Semantic Segmentation Accuracy

As shown in Figure 10, the semantic segmentation results using RGB bands as input demonstrate that, despite relying solely on three visible channels, the model maintains relatively stable segmentation performance across different experimental dates, with mIoU values of 81.71%, 84.43%, and 83.39%, respectively. Overall, the canopy class consistently achieves the highest IoU, exceeding 0.91 on all three dates, indicating that RGB bands can effectively capture the texture, chromatic, and spectral differences of the cotton canopy in the visible region and thus provide good class separability. In contrast, the discrimination between plastic mulch and bare soil is relatively lower and exhibits some temporal variability, with IoU values for plastic mulch ranging from 0.73 to 0.76 and those for bare soil ranging from 0.80 to 0.83. This performance degradation may be attributed to the limited spectral contrast between the two classes in the visible region, brightness fluctuations caused by surface moisture evaporation, and reflectance variations under different illumination conditions. Consequently, RGB-based models are more susceptible to external factors when identifying non-vegetation classes.

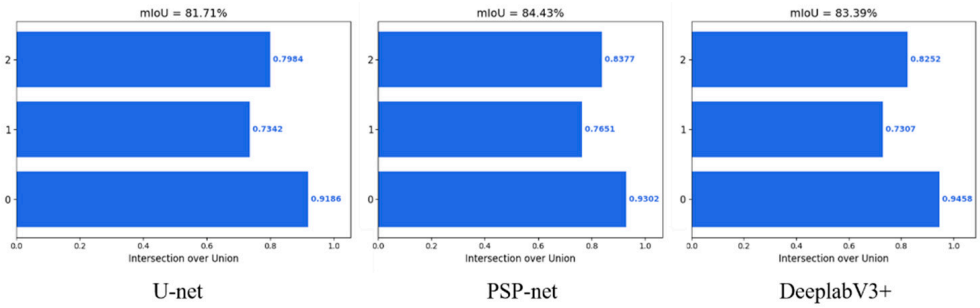


Figure 10. Accuracy validation of visible-color images using three semantic segmentation models (0: canopy; 1: plastic mulch; 2: bare soil).

It is noteworthy that the overall mIoU values of the three models remain above 80%, indicating that RGB-based models can already achieve a reasonable baseline segmentation performance in high-resolution imagery of mulched cotton fields. However, compared with the separability achieved by two-band indices derived from hyperspectral feature selection, RGB-based models remain limited in their ability to capture spectral differences between plastic mulch and bare soil in the near-infrared and shortwave infrared regions, making confusion between these two classes unavoidable. This observation further confirms the importance of constructing spectral band indices with high separability, particularly within the key sensitive regions of 700–900 nm and 400–600 nm. By selecting the most discriminative band combinations, the separability between plastic mulch and bare soil can be substantially improved, thereby enhancing the stability of semantic segmentation models applied to UAV remote sensing imagery of mulched cotton fields.

After being incorporated into semantic segmentation model training, the optimal single-band or two-band combinations selected based on JM separability analysis among different class pairs consistently achieved superior segmentation performance compared with the RGB three-band model (Figure 11), demonstrating the effectiveness of separability-based feature selection in mulched cotton field scenarios. In terms of overall accuracy, the three models achieved mIoU values of 83.76%, 85.86%, and 85.81%, respectively, representing varying degrees of improvement over the RGB baseline (81.71–84.43%). Among the three models, PSPNet achieved the highest mIoU value (85.86%), indicating its stronger capability to discriminate among canopy, plastic mulch, and bare soil. Moreover, the segmentation results of all three models are consistent with the high-separability character-

istics identified in the preceding JM analyses of single-band and two-band indices, further validating the reliability of the band selection strategy based on separability metrics.

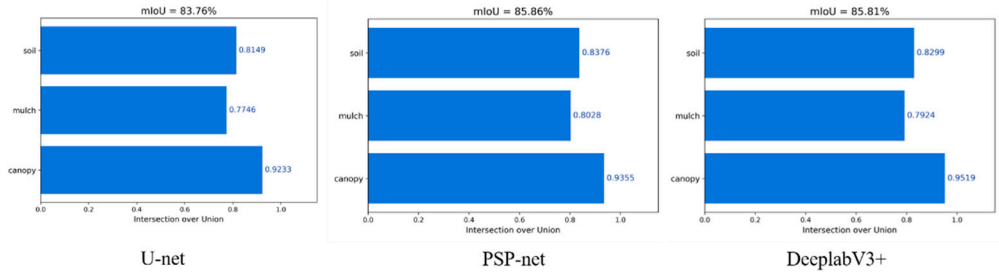


Figure 11. Accuracy validation of optimal band-combination images using three semantic segmentation models.

In terms of class-wise performance, the canopy class consistently achieves the highest IoU values across all models (0.9233–0.9519), which is consistent with its pronounced spectral reflectance variation across growth stages and relatively stable textural structure. In addition, the canopy class exhibits consistently high JM values across different spectral indices and band combinations, making it the easiest class to be stably classified by the models. The IoU values for the bare soil class (0.8149–0.8376) are generally comparable to or slightly higher than those obtained using the RGB model, indicating that optimized band combinations better capture spectral differences in areas with relatively low surface cover. By contrast, the plastic mulch class shows the most substantial improvement in IoU (0.7746–0.8028), representing a stable increase compared with the RGB-based results (0.734–0.765). This improvement is closely associated with the high separability of the selected two-band indices and single-band spectral features for both the mulch–canopy and mulch–soil class pairs, demonstrating that the proposed band selection strategy significantly enhances the model's ability to discriminate plastic mulch.

In addition to the date-wise validation, we performed a paired Wilcoxon signed-rank test as a supplementary significance check on a randomly sampled subset of test images (n = 10), using the per-image IoU of the plastic-mulch class (Class 1). Although the subset's absolute mIoU may deviate from the overall test-set mean due to the small sample size, the paired design evaluates within-image differences (OPT–RGB) and is therefore less affected by between-image variability. Nevertheless, given the small n, the resulting p-value (e.g., $p = 0.015625$ for PSPNet) should be interpreted as an indicative statistical snapshot rather than a fully generalizable inference for the entire dataset. The optimal inputs provided the most evident benefit for PSPNet (RGB vs. optimal mIoU: 0.7189 ± 0.0336 vs. 0.7544 ± 0.0290; W = 0.0000, $p = 0.015625$; mean gain 0.0392), whereas DeepLabV3+ and U-Net showed comparable performance to RGB on this subset (mean gains of +0.0174 and -0.0102, respectively). Future work will extend the paired significance analysis to the full test set or via repeated resampling/bootstrapping to provide more robust uncertainty estimates.

Overall, using the optimal spectral bands and two-band indices selected based on separability assessment as model inputs not only outperforms the RGB-based model in terms of overall accuracy, but also substantially improves the classification performance of challenging classes such as plastic mulch and bare soil. As shown in Figure 12, we can see the plastic mulch identification results. These results further highlight the critical role of spectral features in semantic segmentation under complex mulched cotton field conditions.

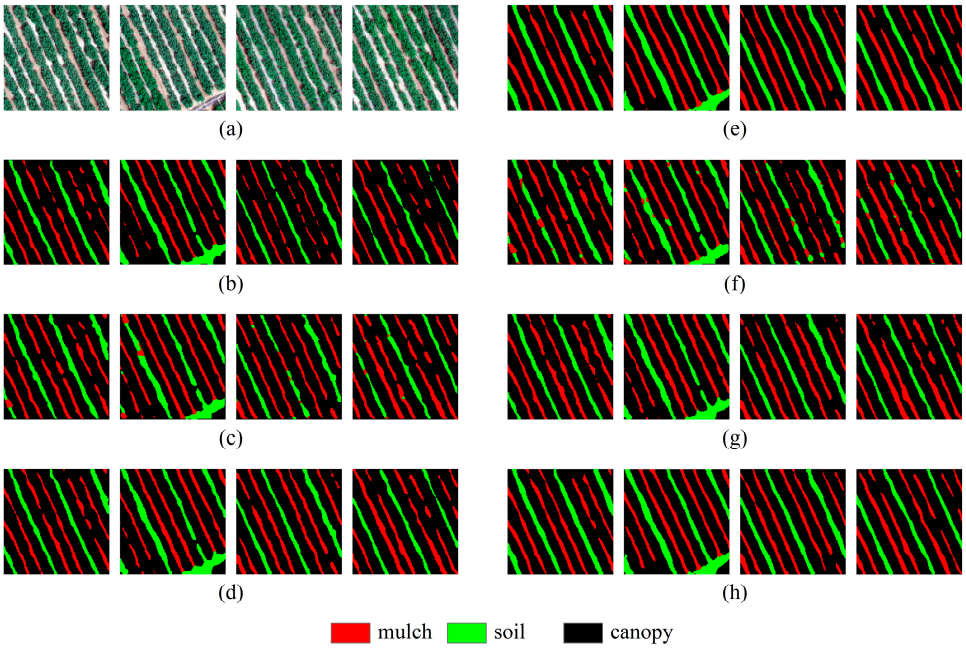


Figure 12. Plastic mulch identification results in mulched cotton fields based on UAV hyperspectral imagery. (**a**) RGB image; (**b**) Label image; (**c**) PSPNet with optimal band-combination; (**d**) DeepLabV3+ with optimal band-combination; (**e**) UNet with optimal band-combination; (**f**) PSPNet with RGB; (**g**) DeepLabV3+ with RGB; (**h**) UNet with RGB.

4. Discussion

4.1. Single-Band Spectral Reflectance Characteristics

By analyzing the reflectance spectra of plastic mulch, bare soil, and canopy across different growth stages, this study demonstrates that the three surface types maintain stable and pronounced spectral differences from the visible to near-infrared regions, providing a solid physical basis for subsequent construction of separability indices and spectral band selection. Such spectral divergence is consistent with the fundamentally different optical properties and structural characteristics of vegetation, polymer-based mulch materials, and exposed soil surfaces, highlighting the advantage of hyperspectral data in fine-scale surface characterization compared with multispectral or RGB imagery [40]. From an agronomic perspective, these physically grounded contrasts enable field-scale mapping of mulch coverage and exposed soil patches, which is directly relevant to evaluating mulching effectiveness (e.g., coverage integrity and potential exposure hotspots) and supporting operational monitoring of residual plastic pollution.

Nevertheless, it is important to emphasize that these spectral differences are not solely governed by the intrinsic properties of the surface materials. Instead, they are jointly modulated by a range of external and biophysical factors, including illumination geometry, soil moisture conditions, the degree of plastic mulch aging and contamination, as well as temporal variations in cotton leaf area index (LAI) [41]. For instance, the rapid increase in canopy reflectance in the near-infrared region during crop development reflects changes in canopy architecture, cellular structure, and leaf water content, which are well-known drivers of vegetation spectral behavior [42]. In contrast, the persistently high reflectance of plastic mulch in the visible region may be influenced not only by its material composition, but also by surface dust accumulation, photodegradation, and cumulative solar exposure over time [43]. Seasonal variations in bare soil spectra are more closely associated with soil moisture evaporation dynamics, surface roughness, and micro-scale crust formation, all of which can alter soil reflectance independently of soil texture or composition [44]. As a result, although the overall spectral trends of the three surface types remain relatively

stable at a macroscopic level, their absolute reflectance values and local spectral features may vary across observation dates and environmental conditions.

Notably, the short-wavelength range around 400–420 nm (with 402 nm emerging as a highly discriminative single band) appears particularly sensitive for separating mulch from soil. This can be explained by the combined effects of relatively strong absorption of bare soil in the blue/near-UV edge (influenced by soil constituents such as iron oxides and organic matter and further suppressed under higher soil moisture) and the scattering/specular behavior of polymer films that can maintain comparatively higher apparent reflectance in this range. In addition, agricultural plastic films are often manufactured with stabilizers, pigments, and UV-related additives to improve durability and regulate radiative properties, which may also contribute to short-wavelength optical differences. Because the exact formulation of the films used in this study was not chemically characterized, the observed separability is interpreted as primarily driven by the fundamental soil–polymer contrast at short wavelengths, while additive effects remain a plausible contributing factor that warrants targeted verification through controlled laboratory spectra of representative film samples (new vs. aged/dust-contaminated).

These findings suggest that while single-band spectral characteristics provide valuable insights into class separability, they also exhibit a degree of conditional dependence. Consequently, the optimal discriminative bands identified in this study may require adjustment when applied to different years, management practices, or soil backgrounds. Overall, the spectral analysis highlights pronounced physical differences among canopy, plastic mulch, and bare soil, thereby establishing a robust theoretical foundation for separability-based feature selection and model development. At the same time, the observed temporal and environmental sensitivity underscores the necessity of incorporating additional contextual information or normalization strategies to enhance spectral robustness across time and space, especially for operational monitoring scenarios.

4.2. JM Distance Analysis of Single-Band and Two-Band Indices

The single-band JM separability analysis demonstrates that the mulch–soil, mulch–canopy, and soil–canopy class pairs exhibit pronounced differences across different spectral ranges, highlighting the advantage of hyperspectral data in fine-scale surface characterization [45]. Compared with multispectral or RGB imagery, hyperspectral measurements provide continuous spectral information that allows subtle reflectance differences among surface materials to be quantified more precisely, particularly in heterogeneous agricultural environments such as mulched cotton fields. In practical terms, the JM-driven analysis offers an interpretable basis for identifying minimal yet informative spectral features, which can support lightweight configurations for routine monitoring when full hyperspectral acquisition is not feasible.

At the same time, variations in JM values across wavelengths also reveal that certain spectral bands are more sensitive to spectral noise and environmental disturbances. For example, the commonly observed decrease in separability for the mulch–soil class pair around 720 nm is likely associated with a combination of increased plastic mulch transparency and the gradual rise in bare soil reflectance at this wavelength. As canopy cover increases and mulch exposure decreases, the optical contribution of the underlying soil becomes more pronounced, leading to spectral convergence between mulch and soil in this transitional spectral region. This phenomenon suggests that not all wavelengths contribute equally to class discrimination, even when overall spectral contrast exists [46]. In contrast, enhanced separability in the near-infrared region—where the mulch–canopy and soil–canopy class pairs consistently maintain JM values close to 2.0—indicates that plant structural characteristics dominate spectral behavior in this region. Although near-infrared

bands are generally more sensitive to illumination variability, atmospheric conditions, and bidirectional reflectance effects, the reflectance mechanisms driven by canopy internal structure, leaf arrangement, and water content far outweigh external disturbances. As a result, these bands exhibit relatively high and stable separability across observation dates, making them particularly valuable for vegetation-related discrimination tasks [42].

It should be noted, however, that the JM distance is a statistical metric derived from within-class variance and between-class distance, which makes it inherently sensitive to sampling density, spectral homogeneity, and noise levels. In practical applications, minor variations in spectral curve shapes caused by sensor noise, illumination fluctuations, or limited sample representativeness may be amplified in JM distance curves. Similar sensitivity of spectral separability measures to noise has been reported in previous remote sensing studies [46], suggesting that JM-based analyses benefit from appropriate denoising, smoothing, or spectral normalization procedures.

The analysis of two-band spectral indices further confirms the potential of specific band combinations to enhance spectral separability. By integrating information from two wavelengths, indices can emphasize particular spectral contrasts while suppressing redundant or irrelevant information. Nevertheless, the variability of index performance across growth stages and class pairs also highlights the inherent limitations of two-band indices.

First, index construction relies on inter-band differences or ratios. When the spectral curves of different surface types are simultaneously influenced by external factors—such as soil moisture fluctuations or overall reflectance increases due to plastic mulch aging—the resulting indices may be synchronously affected, leading to reduced separability. Under such conditions, indices may fail to distinguish between classes even when absolute reflectance differences remain.

Second, for the mulch–soil class pair, indices such as DI and NDI generally exhibit relatively low separability. This result suggests that the intrinsic spectral contrast between plastic mulch and bare soil across the full spectral range is inherently limited, and that index-based transformations cannot artificially generate separability where fundamental spectral differences are weak [47,48]. In this sense, two-band indices should be viewed as tools for enhancing existing contrast rather than creating new discriminatory information.

Third, differences among indices reflect the sensitivity of their mathematical formulations to spectral shape. For instance, DI tends to be more responsive to local reflectance variations and slope changes, which explains the pronounced fluctuations observed in its separability heatmaps across growth stages. In contrast, ratio-based indices such as NDI, LRI and RI benefit from normalization effects that reduce sensitivity to absolute reflectance magnitude, resulting in greater stability across dates and environmental conditions [47]. This normalization can partially cancel scene-wide brightness drift caused by varying solar angles and moisture-driven changes in surface reflectance, thereby improving temporal robustness. This distinction underscores the importance of selecting index formulations that align with the temporal and environmental characteristics of the study area.

It should be emphasized that high index-based separability does not necessarily guarantee improved model performance. While indices can highlight specific spectral contrasts, they may also compress spectral information by retaining only difference- or ratio-based features, potentially discarding complementary information present in the original spectra. Therefore, index selection should be guided not only by separability metrics, but also by downstream model requirements.

Overall, the single-band JM analysis indicates that bands with high separability tend to exhibit relatively stable cross-period performance, although the spectral mechanisms underlying different separability patterns warrant further investigation. In practical model training, spectral indices and multi-band combinations should be used in a complementary

manner to fully exploit the richness of hyperspectral information. Taken together, while two-band indices are effective in capturing key spectral differences, their stability and sensitivity must be comprehensively evaluated in relation to crop growth stages and environmental conditions to ensure robust and transferable model performance. The JM-driven band/index screening provides an interpretable pathway to derive lightweight spectral configurations (single band or two-band indices) that can reduce sensor complexity and facilitate cost-effective operational deployment. For transfer to other mulched cropping systems such as maize and vegetable fields, the same "separability analysis → feature screening" step can be repeated with a small number of representative samples under local soil moisture and illumination conditions, ensuring that the selected features remain robust across crop growth stages.

4.3. Impact of JM-Selected Inputs

A comparison between the RGB-based model and the feature-selected multi-band combination models clearly indicates that spectral feature enhancement can effectively improve the recognition of specific surface classes, particularly for targets such as plastic mulch and bare soil, which exhibit relatively similar spectral appearances in the visible domain but fundamentally different physical properties. This improvement demonstrates that incorporating discriminative spectral information beyond the visible range is essential for resolving class ambiguities commonly encountered in complex agricultural scenes. From an application standpoint, the most valuable gain lies in improving the segmentation of plastic mulch, as it supports more reliable identification of residual plastic hotspots and reduces uncertainty when prioritizing cleanup operations or evaluating recovery measures.

Nevertheless, the RGB-based model retains several inherent advantages that should not be overlooked. RGB imagery is widely available, cost-effective to acquire, and computationally efficient to process, which contributes to stable model convergence and robust learning behavior. In addition, high-resolution RGB data contain rich textural and structural cues, enabling consistently strong performance in canopy identification. Vegetation canopies typically exhibit distinctive textures, color patterns, and spatial continuity in RGB images, allowing deep learning models to reliably extract discriminative features even in the absence of near-infrared information [49].

At the same time, the limitations of RGB-based approaches are also evident. Without access to near-infrared spectral information, RGB models are constrained to rely primarily on brightness and color differences for class discrimination. Under conditions such as high-reflectance backgrounds, moist soil surfaces, or shadowed areas, the visual contrast between plastic mulch and bare soil is often reduced, increasing the likelihood of misclassification. These limitations are particularly pronounced in early growth stages or partially covered fields, where mixed visual patterns and heterogeneous illumination further complicate class separation.

By contrast, multi-band combination models leverage key spectral bands selected through JM separability and spectral index analyses (e.g., 400–500 nm and 700–900 nm), which physically amplify class-specific spectral differences in a targeted manner. The inclusion of near-infrared bands enables the model to capture vegetation structural signals and moisture-related spectral responses that are not accessible in RGB imagery. As a result, the separability between plastic mulch and bare soil is significantly improved, leading to more stable and accurate segmentation results across different observation dates.

However, the benefits of multi-band inputs are accompanied by certain trade-offs. Despite the overall improvement in mIoU, multi-band models inevitably involve increased input dimensionality and computational complexity, which may lead to higher training costs and longer inference times. Moreover, hyperspectral or multi-band data are inherently

more sensitive to spectral noise, sensor calibration errors, and illumination variability, particularly under unstable field conditions. These factors may introduce greater prediction uncertainty if not properly addressed through preprocessing or model regularization.

Compared with existing UAV-based plastic film studies, our results fall within the range of reported deep-learning segmentation performance while addressing a more challenging in-season, multi-class scenario (plastic mulch–bare soil–canopy) with strong spectral confusion between mulch and bright soil. For example, in pre-sowing cotton fields where the task is often formulated as binary residual-film versus background segmentation, Zhai et al. [50] reported an mIoU of 87.53% using a modified U-Net, whereas a pixel-block machine-learning baseline achieved only 71.25% mIoU. In addition, early UAV studies on plastic-mulched farmland mapping have reported high recognition performance under simpler settings (e.g., SegNet achieving up to 88.68% overall accuracy using a single near-infrared band at 900 nm), although such accuracy values are not directly comparable to IoU-based metrics used in this study [39]. In contrast, our study targets three-class mapping during crop growth stages, where mulch exposure dynamics, dust accumulation, and illumination-driven soil brightness variations jointly increase the difficulty of separating mulch from soil; under this setting, the proposed JM-driven band/index selection consistently improves mulch IoU relative to RGB-only inputs, demonstrating the benefit of interpretable separability-guided feature design.

Therefore, practical deployment of multi-band semantic segmentation models should balance segmentation accuracy with data acquisition cost, spectral stability, and model complexity. Rather than relying exclusively on either RGB or hyperspectral inputs, future studies may benefit from hybrid strategies that integrate spectral features, index-based features, and spatial–textural information within unified deep learning frameworks. Such approaches could exploit the complementary strengths of different data modalities while mitigating their individual limitations. The paired statistical comparison further suggests that the optimal-band inputs can yield architecture-dependent benefits, with PSPNet showing the most pronounced and statistically supported improvement for the mulch class. This advantage is plausibly linked to PSPNet's Pyramid Pooling Module, which aggregates multi-scale contextual information and strengthens global-scene understanding: in mulched cotton fields, plastic film often forms large, continuous belts aligned with row geometry, whereas bare soil tends to appear as fragmented inter-row patches or locally exposed areas. By pooling features at multiple spatial scales, PSPNet can better capture long-range continuity and field-level layout, thereby reducing confusion between visually similar bright soil patches and plastic mulch, especially under heterogeneous illumination and partial canopy cover. These observations indicate that both feature design and model choice should be considered when transferring the pipeline to other crop systems.

Overall, the results of this study not only confirm the value of hyperspectral separability analysis for improving semantic segmentation performance, but also provide an interpretable theoretical basis for developing band selection strategies in UAV-based remote sensing monitoring of mulched cotton fields. These findings highlight the importance of coupling physically meaningful spectral feature selection with deep learning architectures to achieve accurate, robust, and application-oriented segmentation outcomes in complex agricultural environments.

4.4. Limitations and Future Perspectives

Although this study demonstrates the effectiveness of integrating hyperspectral separability analysis with deep learning-based semantic segmentation, the experiments were conducted in a single region in Alar, Xinjiang, under relatively consistent management practices and environmental conditions. As soil backgrounds (texture, salinity, mineral

composition), irrigation regimes, mulch materials, and crop varieties change, both spectral contrast patterns and JM-based band/index rankings may shift, potentially affecting model generalization. A concrete future direction is to conduct multi-regional validation across contrasting soil and management conditions and establish a small cross-site calibration dataset to re-estimate separability and update the feature configuration accordingly. This is particularly important for extending the framework to other mulched systems such as maize ridge–furrow mulching and vegetable full-bed mulching, where planting geometry and background soil exposure differ from cotton fields.

In addition, hyperspectral UAV measurements are sensitive to illumination geometry, radiometric calibration uncertainty, and sensor noise, which can propagate into separability curves and lead to prediction instability under variable field conditions. While careful acquisition and preprocessing were performed, residual illumination induced variability may still influence separability metrics and segmentation outcomes. Future work will integrate standardized reflectance calibration (e.g., reference-panel-based correction), spectral normalization, and, where feasible, BRDF-aware adjustments to reduce lighting-related spectral drift. Moreover, when scaling the workflow to multi-region or multi-season datasets, additional scene-to-scene radiometric harmonization may be needed to ensure cross-site comparability; practical options include pseudo-invariant feature (PIF)-based relative normalization and dark object subtraction (DOS) to mitigate inter-scene radiometric shifts prior to separability analysis and model inference. Incorporating physically informed normalization or radiative transfer-based constraints is also a promising route to enhance temporal robustness and support operational deployment.

Film condition represents another practical source of uncertainty. Spectral behavior in short-wavelength regions (including 400–420 nm) can be affected by film aging, dust contamination, and mechanical damage, which may lower apparent film reflectance and increase within-class variance. In this study, we did not explicitly log the film "age" as days since deployment for each plot and therefore did not perform an age-stratified evaluation. Nevertheless, because the dataset spans multiple observation dates and growth stages, it inevitably captures heterogeneous film appearances, from relatively clean or intact areas to locally dust-covered or torn patches; thus, the reported performance reflects aggregated variability rather than a single uniform film state. Future work will strengthen robustness analysis by adopting a lightweight field protocol that records film-condition attributes alongside polygon labels. Specifically, during ground-truthing we will (i) manually categorize each film polygon into a small set of condition classes (e.g., fresh/intact, aged/dusty, and torn/fragmented) supported by close-range photos, and (ii) where feasible, derive a simple quantitative "dustiness index" from radiometrically calibrated imagery (e.g., a blue-band brightness/whiteness shift, a blue–red ratio or NDI, or local texture/contrast metrics capturing surface roughening) to reduce subjectivity. These additions will enable condition-stratified evaluations and more reliable assessment of performance consistency across degradation levels, and they can further support condition-aware training or reweighting to improve generalization when transferring the workflow to diverse cropping systems and management scenarios.

Finally, practical deployment requires balancing accuracy, cost, and computational efficiency. Full hyperspectral acquisition and high-dimensional multi-band inference can be challenging for routine large-scale monitoring despite their accuracy benefits. In this regard, the proposed JM-driven feature selection provides a pragmatic compromise: it retains physically interpretable and highly discriminative information using only a minimal set of bands/indices, thereby reducing input dimensionality and computational burden while maintaining strong segmentation performance. Although it would be informative to include a "brute-force" baseline using all hyperspectral bands or a PCA-reduced representa-

tion, directly feeding tens to hundreds of highly correlated spectral channels into semantic segmentation networks substantially increases memory and computation requirements and may introduce redundancy-driven instability and overfitting, particularly when training data are limited. Therefore, our emphasis is not only on maximizing accuracy but also on developing an interpretable and deployable configuration that can be transferred across operational settings. In future work, we will benchmark the proposed feature selection against PCA-based hyperspectral reductions and, where feasible, full-band inputs, and further explore end-to-end spectral compression modules (e.g., 1×1 convolutional projections or attention-based spectral weighting) to better balance accuracy, robustness, and efficiency for scalable mulch monitoring and plastic waste management.

5. Conclusions

Based on UAV hyperspectral imagery acquired over mulched cotton fields in Alar, Xinjiang, this study systematically developed a complete technical framework for fine-scale plastic mulch identification in agricultural fields, encompassing spectral separability evaluation, two-band index construction, and deep learning-based semantic segmentation optimization. The main conclusions are summarized as follows:

(1) The three major surface types in mulched cotton fields—canopy, plastic mulch, and bare soil—exhibit stable and pronounced spectral differences from the visible to near-infrared regions, providing a reliable basis for subsequent feature construction and band optimization. Spectral analysis shows that canopy reflectance is highest in the red-edge and near-infrared regions, while plastic mulch exhibits significantly higher brightness than bare soil in the visible region. Overall, good spectral separability among the three classes is observed across the 400–1000 nm range.

(2) The JM separability analysis clearly identifies key sensitive spectral regions for different class pairs, primarily concentrated in the 400–500 nm and 700–900 nm ranges. High separability is consistently observed for the plastic mulch–canopy and bare soil–canopy pairs in both the visible and near-infrared regions, whereas separability for the plastic mulch–bare soil pair remains relatively weak, indicating that enhancing spectral contrast between these two classes is a critical step for accurate plastic mulch identification.

(3) Four spectral indices (DI, RI, NDI, and LRI) constructed from full-band combinations significantly enhance inter-class spectral differences and enable the identification of optimal band combinations. Deep learning semantic segmentation models (U-Net, DeepLabV3+, and PSPNet) trained using these optimal spectral inputs consistently outperform RGB-based models, with PSPNet achieving the best overall performance, particularly exhibiting the most pronounced improvement in IoU for the plastic mulch class.

In summary, this study establishes an integrated plastic mulch identification framework for mulched cotton fields by combining spectral separability evaluation, two-band index optimization, and deep learning-based semantic segmentation, providing a feasible technical pathway for high-accuracy and automated UAV-based plastic mulch monitoring. The proposed framework enables effective discrimination of key surface components, including plastic mulch, bare soil, and canopy, at fine spatial scales, thereby offering important technical support for residual plastic pollution monitoring and precision agricultural management. Considering the heterogeneity of regional environments and the complexity of spectral conditions, future research may further integrate multi-temporal observations, spectral normalization techniques, and multimodal data fusion strategies to enhance model stability and generalization across diverse agricultural settings.

https://doi.org/10.3390/agronomy16040458

Author Contributions: Q.Z.: Investigation, Formal analysis, Data curation, Writing—original draft; S.L.: Investigation; F.G.: Investigation; H.N.: Software; D.D.: Software; P.Z.: Software; N.L.: Methodology; Y.S.: Investigation; C.L.: Methodology, Funding acquisition; H.L.: Writing—review and editing, Funding acquisition. All authors have read and agreed to the published version of the manuscript.

Funding: This work was funded by the Technology Innovation Program (ASTIP), Chinese Academy of Agricultural Sciences.

Data Availability Statement: The datasets presented in this article are not readily available because the data are part of an ongoing study.

Conflicts of Interest: The authors declare that they have no known competing financial interests or personal relationships that could have appeared to influence the work reported in this paper.

References

1. Li, H.; Kuang, N.; Gou, Q.; Ma, Y.; Li, Q. Effects of Different Film Mulches on Photosynthetic Characteristics and Yield of Summer Maize (*Zea mays* L.) in the North China Plain. *Arch. Agron. Soil Sci.* **2021**, *67*, 179–190. [CrossRef]
2. Yang, Y.; Zhou, X.; Yang, Y.; Bi, S.; Yang, X.; Li Liu, D. Evaluating Water-Saving Efficiency of Plastic Mulching in Northwest China Using Remote Sensing and SEBAL. *Agric. Water Manag.* **2018**, *209*, 240–248. [CrossRef]
3. Qin, X.; Li, Y.; Han, Y.; Hu, Y.; Li, Y.; Wen, X.; Liao, Y.; Siddique, K.H. Ridge-Furrow Mulching with Black Plastic Film Improves Maize Yield More than White Plastic Film in Dry Areas with Adequate Accumulated Temperature. *Agric. For. Meteorol.* **2018**, *262*, 206–214. [CrossRef]
4. Yan, C.; Liu, E.; Shu, F.; Liu, Q.; Liu, S.; He, W. Review of Agricultural Plastic Mulching and Its Residual Pollution and Prevention Measures in China. *J. Agric. Resour. Environ.* **2014**, *31*, 95.
5. Zhang, J.; Ren, S.; Dai, J.; Ding, F.; Xiao, M.; Liu, X.; Yan, C.; Ge, T.; Wang, J.; Liu, Q. Influence of Plastic Film on Agricultural Production and Its Pollution Control. *Sci. Agric. Sin.* **2022**, *55*, 3983–3996.
6. Wang, Y.; Feng, Z. Temporal and Spatial Variations in Mulch Film Usage across Prefecture-Level Cities in China from 2010 to 2015. *J. Agric. Resour. Environ.* **2022**, *39*, 36–45.
7. Li, C.; Sun, M.; Xu, X.; Zhang, L. Characteristics and Influencing Factors of Mulch Film Use for Pollution Control in China: Microcosmic Evidence from Smallholder Farmers. *Resour. Conserv. Recycl.* **2021**, *164*, 105222. [CrossRef]
8. Hou, L.Q.; Zhang, J.; Zhai, X.L. Social Norms, Ecological Cognition and Farmers' Behavior of Plastic Film Recycling. *J. Arid Land Resour. Environ.* **2019**, *33*, 54–59.
9. Xu, Y.; Fang, S.; Ma, X.; Zhu, Q. Prevention and Control Strategy for the Pollution of Agricultural Plastic Film. *Strateg. Study Chin. Acad. Eng.* **2018**, *20*, 96–102.
10. Liu, E.K.; He, W.Q.; Yan, C.R. 'White Revolution' to 'White Pollution'—Agricultural Plastic Film Mulch in China. *Environ. Res. Lett.* **2014**, *9*, 091001. [CrossRef]
11. Li, H.; Liu, Q.; Mingdong, Z.; Wu, H.; Liu, X.; Xuemei, X.; He, W. Characteristics of Mulching Film Residue Pollution in Farmland and Its Influencing Factors in Xinjiang Region. *J. Agric. Resour. Environ.* **2024**, *41*, 656.
12. Kumar, M.; Xiong, X.; He, M.; Tsang, D.C.; Gupta, J.; Khan, E.; Harrad, S.; Hou, D.; Ok, Y.S.; Bolan, N.S. Microplastics as Pollutants in Agricultural Soils. *Environ. Pollut.* **2020**, *265*, 114980. [CrossRef] [PubMed]
13. Liu, M.; Zheng, X.; Qiang, L.; Li, L.; Zhang, R.; Wang, J. Analysis on the Change of Agricultural Film Usage and the Pollution of Agricultural Film Microplastics in China during Years from 1994 to 2020. *Ecol. Environ.* **2023**, *32*, 2050.
14. Han, J.; Jia, Z.; Wu, W.; Li, C.; Han, Q.; Zhang, J. Modeling Impacts of Film Mulching on Rainfed Crop Yield in Northern China with DNDC. *Field Crops Res.* **2014**, *155*, 202–212. [CrossRef]
15. Veettil, B.K.; Van, D.D.; Quang, N.X.; Hoai, P.N. Remote Sensing of Plastic-covered Greenhouses and Plastic-mulched Farmlands: Current Trends and Future Perspectives. *Land Degrad. Dev.* **2023**, *34*, 591–609. [CrossRef]
16. Hasituya; Chen, Z.; Wang, L.; Wu, W.; Jiang, Z.; Li, H. Monitoring Plastic-Mulched Farmland by Landsat-8 OLI Imagery Using Spectral and Textural Features. *Remote Sens.* **2016**, *8*, 353. [CrossRef]
17. Lu, L.; Di, L.; Ye, Y. A Decision-Tree Classifier for Extracting Transparent Plastic-Mulched Landcover from Landsat-5 TM Images. *IEEE J. Sel. Top. Appl. Earth Obs. Remote Sens.* **2014**, *7*, 4548–4558. [CrossRef]
18. Hasituya; Chen, Z.; Li, F. Hongmei Mapping Plastic-Mulched Farmland with C-Band Full Polarization SAR Remote Sensing Data. *Remote Sens.* **2017**, *9*, 1264. [CrossRef]
19. Lu, L.; Hang, D.; Di, L. Threshold Model for Detecting Transparent Plastic-Mulched Landcover Using Moderate-Resolution Imaging Spectroradiometer Time Series Data: A Case Study in Southern Xinjiang, China. *J. Appl. Remote Sens.* **2015**, *9*, 097094. [CrossRef]

20. Hasituya; Chen, Z.; Wang, L.; Liu, J. Selecting Appropriate Spatial Scale for Mapping Plastic-Mulched Farmland with Satellite Remote Sensing Imagery. *Remote Sens.* **2017**, *9*, 265. [CrossRef]
21. Hasituya; Chen, Z. Mapping Plastic-Mulched Farmland with Multi-Temporal Landsat-8 Data. *Remote Sens.* **2017**, *9*, 557. [CrossRef]
22. Ning, J.; Ni, J.; He, J.; Li, L.; Zhao, Z.; Zhang, Z. Convolutional Attention Based Plastic Mulching Farmland Identification via UAV Multispectral Remote Sensing Image. *Trans. Chin. Soc. Agric. Mach.* **2021**, *52*, 213–220.
23. Huang, H.; Wu, X.; Zhang, K.; Zhang, Z.; Xiao, Y. Research on Field Membrane Recognition Based on Hyperspectral Remote Sensing Technology. *Comput. Digit. Eng.* **2024**, *52*, 541–547.
24. Wu, X.M.; Liang, C.J.; Zhang, D.B.; Yu, L.H.; Zhang, F.G. Identification Method of Plastic Film Residue Based on UAV Remote Sensing Images. *Trans. CSAM* **2020**, *51*, 189–195.
25. Wang, H.; Zhang, X.; Du, S.; Bai, L.; Liu, B. Mapping Annual Urban Evolution Process (2001–2018) at 250 m: A Normalized Multi-Objective Deep Learning Regression. *Remote Sens. Environ.* **2022**, *278*, 113088. [CrossRef]
26. Zhao, M.; Meng, Q.; Wang, L.; Zhang, L.; Hu, X.; Shi, W. Towards Robust Classification of Multi-View Remote Sensing Images with Partial Data Availability. *Remote Sens. Environ.* **2024**, *306*, 114112. [CrossRef]
27. Valman, S.J.; Boyd, D.S.; Carbonneau, P.E.; Johnson, M.F.; Dugdale, S.J. An AI Approach to Operationalise Global Daily PlanetScope Satellite Imagery for River Water Masking. *Remote Sens. Environ.* **2024**, *301*, 113932. [CrossRef]
28. Li, Z.; Weng, Q.; Zhou, Y.; Dou, P.; Ding, X. Learning Spectral-Indices-Fused Deep Models for Time-Series Land Use and Land Cover Mapping in Cloud-Prone Areas: The Case of Pearl River Delta. *Remote Sens. Environ.* **2024**, *308*, 114190. [CrossRef]
29. Xu, Y.; Lu, L. An Attention-Fused Deep Learning Model for Accurately Monitoring Cage and Raft Aquaculture at Large-Scale Using Sentinel-2 Data. *IEEE J. Sel. Top. Appl. Earth Obs. Remote Sens.* **2024**, *17*, 9099–9109. [CrossRef]
30. Shelhamer, E.; Long, J.; Darrell, T. Fully Convolutional Networks for Semantic Segmentation. *IEEE Trans. Pattern Anal. Mach. Intell.* **2017**, *39*, 640–651. [CrossRef]
31. Garcia-Garcia, A.; Orts-Escolano, S.; Oprea, S.; Villena-Martinez, V.; Garcia-Rodriguez, J. A Review on Deep Learning Techniques Applied to Semantic Segmentation. *arXiv* **2020**, arXiv:170406857.
32. Li, R.; Liu, W.; Yang, L.; Sun, S.; Hu, W.; Zhang, F.; Li, W. DeepUNet: A Deep Fully Convolutional Network for Pixel-Level Sea-Land Segmentation. *IEEE J. Sel. Top. Appl. Earth Obs. Remote Sens.* **2018**, *11*, 3954–3962. [CrossRef]
33. Fu, G.; Liu, C.; Zhou, R.; Sun, T.; Zhang, Q. Classification for High Resolution Remote Sensing Imagery Using a Fully Convolutional Network. *Remote Sens.* **2017**, *9*, 498. [CrossRef]
34. Chen, R.; Sun, S. Automatic Extraction of Infrared Remote Sensing Information Based on Deep Learning. *J. Infrared* **2017**, *38*, 37–43.
35. Sherrah, J. Fully Convolutional Networks for Dense Semantic Labelling of High-Resolution Aerial Imagery 2016. *arXiv* **2016**, arXiv:1606.02585.
36. Xu, P.; Wang, P.; Liu, H.; Ning, H.; Wang, J. Evaluation and Application of AquaCrop in Simulation of Alternate Irrigation with Brackish and Fresh Water for Cotton under Mulch Drip Irrigation in Southern Xinjiang. *Ind. Crops Prod.* **2025**, *225*, 120548. [CrossRef]
37. Sen, R.; Goswami, S.; Chakraborty, B. Jeffries-Matusita Distance as a Tool for Feature Selection. In *Proceedings of the 2019 International Conference on Data Science and Engineering (ICDSE), Patna, India, 26–28 September 2019*; IEEE: New York, NY, USA, 2019; pp. 15–20.
38. Ma, Y.; Liu, H.; Chen, Z.; Zhang, K.; Yu, X.; Wang, J.; Sun, J.-S. Canopy Equivalent Water Thickness Estimation of Cotton Based on Hyperspectral Index. *Sci. Agric. Sin.* **2019**, *52*, 4470–4483.
39. Yang, Q.; Liu, M.; Zhang, Z.; Yang, S.; Ning, J.; Han, W. Mapping Plastic Mulched Farmland for High Resolution Images of Unmanned Aerial Vehicle Using Deep Semantic Segmentation. *Remote Sens.* **2019**, *11*, 2008. [CrossRef]
40. Su, H. Dimensionality Reduction for Hyperspectral Remote Sensing: Advances, Challenges, and Prospects. *Natl. Remote Sens. Bull.* **2022**, *26*, 1504–1529. [CrossRef]
41. Atzberger, C. Advances in Remote Sensing of Agriculture: Context Description, Existing Operational Monitoring Systems and Major Information Needs. *Remote Sens.* **2013**, *5*, 949–981. [CrossRef]
42. Jacquemoud, S.; Ustin, S. *Leaf Optical Properties*; Cambridge University Press: Cambridge, UK, 2019.
43. Zhang, M.; Dong, J.; Ge, Q.; Hasituya; Hao, P. A Review of Agricultural Film Mapping: Current Status, Challenges, and Future Directions. *J. Remote Sens.* **2025**, *5*, 0395. [CrossRef]
44. Ustin, S.L.; Gitelson, A.A.; Jacquemoud, S.; Schaepman, M.; Asner, G.P.; Gamon, J.A.; Zarco-Tejada, P. Retrieval of Foliar Information about Plant Pigment Systems from High Resolution Spectroscopy. *Remote Sens. Environ.* **2009**, *113*, S67–S77. [CrossRef]
45. Zhao, Y.; Xu, Z.; Mao, X.; Li, S.; Qi, X.; Che, J. Influence of Film Color, Mulching Ratio and Soil–Mulch Contact Degree on Heat Transfer in Northwest China. *Agric. For. Meteorol.* **2024**, *357*, 110208. [CrossRef]
46. Van der Meer, F. The Effectiveness of Spectral Similarity Measures for the Analysis of Hyperspectral Imagery. *Int. J. Appl. Earth Obs. Geoinf.* **2006**, *8*, 3–17. [CrossRef]

47. Bannari, A.; Morin, D.; Bonn, F.; Huete, A.R. A Review of Vegetation Indices. *Remote Sens. Rev.* **1995**, *13*, 95–120. [CrossRef]
48. Huete, A.R. A Soil-Adjusted Vegetation Index (SAVI). *Remote Sens. Environ.* **1988**, *25*, 295–309. [CrossRef]
49. Ma, L.; Liu, Y.; Zhang, X.; Ye, Y.; Yin, G.; Johnson, B.A. Deep Learning in Remote Sensing Applications: A Meta-Analysis and Review. *ISPRS J. Photogramm. Remote Sens.* **2019**, *152*, 166–177. [CrossRef]
50. Zhai, Z.; Chen, X.; Zhang, R.; Qiu, F.; Meng, Q.; Yang, J.; Wang, H. Evaluation of residual plastic film pollution in pre-sowing cotton field using UAV imaging and semantic segmentation. *Front. Plant Sci.* **2022**, *13*, 991191. [CrossRef] [PubMed]

Disclaimer/Publisher's Note: The statements, opinions and data contained in all publications are solely those of the individual author(s) and contributor(s) and not of MDPI and/or the editor(s). MDPI and/or the editor(s) disclaim responsibility for any injury to people or property resulting from any ideas, methods, instructions or products referred to in the content.